
A Unified Framework for Critical Scaling of Inverse Temperature in Self-Attention

Tomohiro Hayase
AIST

Ryo Karakida
AIST

Abstract

Length-dependent logit rescaling is widely used to stabilize long-context self-attention, but existing analyses and methods suggest conflicting inverse-temperature laws for the context length n , ranging from $(\log n)^{1/2}$ to $\log n$ and $(\log n)^2$. We provide a general theory showing that the desirable scale is determined by the gap-counting function N_n of each attention row. Counting how many competitors lie within each gap from the maximum, we define an upper-tail accumulation scale and prove that it gives the critical inverse-temperature scale for softmax concentration: below this scale, the top competitors remain unseparated, whereas above it, the attention entropy collapses. This framework unifies prior scaling laws as different N_n and yields a direct diagnostic for attention-score families, from idealized theoretical models to more practical transformers.

1 Introduction

Self-attention (Vaswani et al., 2017) is a central component of modern deep learning systems. To understand the mechanism of self-attention, theoretical studies have been actively developed. One standard approach in theoretical analysis is to take large-degree-of-freedom limits, such as the limits of large embedding dimension and large number of heads (Hron et al., 2020; Bordelon et al., 2024; Sakai et al., 2025). In particular, motivated by the practical importance of inference with long contexts, recent work has begun to explore the infinite-context-length limit. For example, long contexts can induce token clustering as metastable states (Geshkovski et al., 2025; Bruno et al., 2025), as well as rank collapse (Nait Saada et al., 2025). Moreover, increasing the inverse temperature with the context length changes the phase from rank collapse to entropy collapse, with a critical scaling separating the two regimes (Giorlandino and Goldt, 2026; Chen et al., 2025).

Despite this progress, our understanding of the desirable scaling for long contexts is limited. The prior theory has identified critical inverse-temperature scalings only in restricted stochastic and deterministic settings, such as Gaussian-logit (i.e., random-energy-style) analyses and equicorrelated self-attention models (Giorlandino and Goldt, 2026; Chen et al., 2025). In practice, inverse temperatures that increase with the context length are also widely used to avoid the instability of inference for long contexts (Bai et al., 2023; Nakanishi, 2025; Peng et al., 2023). As reviewed in Section 2.2, these mechanisms can be placed on a common logarithmic-exponent scale, but the resulting exponents are not consistent across models and arguments. This suggests that the exponent is not determined by context length alone. What is missing is a principle that identifies, from the attention scores themselves, the scale at which softmax changes regime.

This paper develops such a principle through a deterministic gap-counting framework. Instead of organizing an attention row by ordinal rank, we count how many competitors lie within each score gap from the maximum. The exponential growth rate of this counting curve defines a row-wise critical scale, the upper-tail accumulation scale (Definition 4.4). Our main theorem shows that this scale controls the inverse-temperature scale separating the diffuse and concentrated softmax regimes

for arbitrary deterministic score families, without assuming Gaussian logits, independent scores, random initialization, or a special token construction.

The main contribution is a unified gap-counting framework: the cumulative function $N_n(t)$ explains both idealized theoretical models and actual transformers, and yields a calibration principle for the inverse-temperature exponent. The upper-tail accumulation scale Λ_n keeps softmax away from both non-separation of the top competitors and entropy collapse, so any non-degenerate logarithmic schedule has $\xi_\beta = \xi_\Lambda$ (Corollary 4.8); existing temperature rules become different N_n and hence different ξ_Λ , with the legacy $\beta_n \propto \log n$ as the $\xi_\Lambda = 1$ slice. In two complementary settings (inference-time β -sweep at extrapolation lengths and training-time learning of an inverse-temperature vector), $\hat{\xi}_\Lambda$ read directly from attention scores aligns with the empirical optimum ξ_β^* . Section 3 presents the motivating sweeps, and Section 4 develops the deterministic theory and applies its empirical readings to concrete self-attention scores.

2 Preliminaries

2.1 Notation

Let the context length be n . For $n \geq 2$, let $z_{n,1}, \dots, z_{n,n} \in \mathbb{R}$. The softmax probability of token j at inverse temperature $\beta > 0$ is $p_{n,j}(\beta) := e^{\beta z_{n,j}} / \sum_{\ell=1}^n e^{\beta z_{n,\ell}}$. The concrete instance we have in mind is a fixed-query self-attention row of the standard scaled dot-product form (Vaswani et al., 2017),

$$z_{n,j} = \frac{\langle W_n^Q x_{n,i_n}, W_n^K x_{n,j} \rangle}{\sqrt{d_{\text{qk},n}}} = \frac{\langle q_{n,i_n}, k_{n,j} \rangle}{\sqrt{d_{\text{qk},n}}}, \quad (2.1)$$

with token embeddings $x_{n,j} \in \mathbb{R}^{d_n}$, weight matrices $W_n^Q, W_n^K \in \mathbb{R}^{d_{\text{qk},n} \times d_n}$, query/key vectors $q_{n,i} := W_n^Q x_{n,i}$, $k_{n,j} := W_n^K x_{n,j}$, and a fixed query index i_n . The theory below uses only the resulting score sequence $(z_{n,j})_j$, so the embedding-weight factorization is absorbed into q, k from Section 4 onward. For positive sequences, $f_n \sim g_n$ means $f_n/g_n \rightarrow 1$ and $f_n \asymp g_n$ means $c_1 g_n \leq f_n \leq c_2 g_n$ for some constants $0 < c_1 \leq c_2$ and all sufficiently large n . We study the asymptotic regime $n \rightarrow \infty$ with $\beta = \beta_n$, and parametrise scaling laws by the exponent $\xi_\beta \geq 0$ in $\beta_n \asymp (\log n)^{\xi_\beta}$.

2.2 Related work

Prior choices for the softmax inverse temperature in self-attention each fix ξ_β a priori (Table 1). *Gaussian-logit analyses* ($\xi_\beta = 1/2$). Drawing an analogy with the Random Energy Model (Derrida, 1981), Giorlandino and Goldt (2026) conjecture $\beta_n \asymp \sqrt{\log n}$ as the scaling that balances rank and entropy collapse. Under a marginally Gaussian attention-logit assumption, Anson et al. (2025) derive a position-dependent multiplicative factor $a_t \asymp \sqrt{\log t}$ that yields scale-invariant total attention. *Explicit logarithmic temperature* ($\xi_\beta = 1$). SSMAX (Nakanishi, 2025) multiplies attention logits by $s \log n$ with s learned per head, and Qwen (Bai et al., 2023) adopts a length-dependent LogN multiplier of order $\log n / \log n_{\text{train}}$ outside the training window n_{train} . Chen et al. (2025) prove a phase transition at $\beta_n \asymp \log n$ in a deterministic equicorrelated (“simplex”) configuration. *Doubled rescaling* ($\xi_\beta = 2$). YaRN (Peng et al., 2023) multiplies both the query and key sides of the rotary embedding by a common $\log n$ -dependent multiplier, doubling the exponent (Appendix E). The values $\xi_\beta \in \{1/2, 1, 2\}$ are the only ones with widely cited mechanisms; intermediate values appear naturally once ξ_β is treated as a continuous parameter, as in our ξ_β -sweep (Section 3) and our model-free gap-counting theory (Section 4).

ξ_β	Mechanism (prior work)
1/2	Gaussian-logit analyses (Giorlandino and Goldt, 2026; Anson et al., 2025)
1	SSMAX (Nakanishi, 2025), Qwen LogN (Bai et al., 2023); equicorrelated phase transition (Chen et al., 2025)
2	YaRN (Peng et al., 2023)

Table 1: Prior work grouped by the implicit exponent ξ_β in $\beta_n \asymp (\log n)^{\xi_\beta}$.

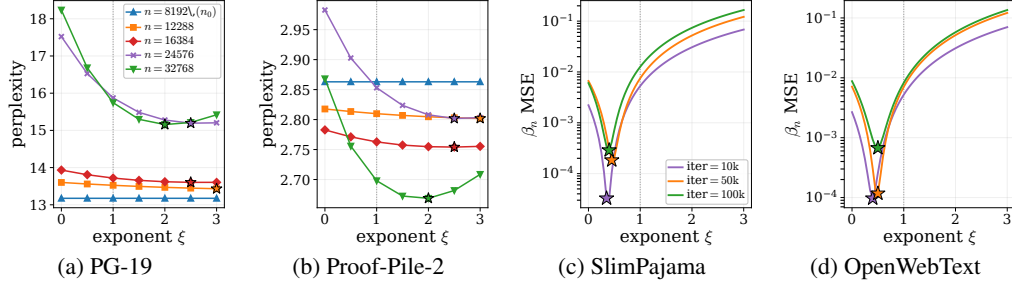


Figure 1: Sweeping ξ_β shows that optima need not occur at $\xi_\beta = 1$. (a, b) Inference-time perplexity (back-half sliding window; Appendix A.2) is minimized around $\xi_\beta^* \in [2, 2.5]$. (c, d) The bias-free least-squares fit of the learned β_n to $a_1(\log n)^{\xi_\beta}$ ($n \geq 64$) has its MSE minimum below $\xi_\beta = 1$ on both datasets. The dotted line marks $\xi_\beta = 1$. Doc-level SE on PPL is at most 10% of the cell mean in (a, b); residual-bootstrap half-IQR on MSE is at most 8% of the point-estimate MSE in (c, d).

3 A minimal empirical check: $\xi_\beta = 1$ is not universal

Prior mechanisms in Table 1 fix the logarithmic inverse-temperature exponent ξ_β a priori. We use the single-parameter ansatz $\beta_n = c(\log n)^{\xi_\beta}$ only as a probe: the goal is to check whether the logarithmic choice $\xi_\beta = 1$ is empirically forced.

Figure 1 gives two complementary checks. Three context-length quantities appear repeatedly below: the per-token context length n of Section 2.1, the *evaluation context length* n_{eval} (the inference sliding-window size, fixed per evaluation, with $n \leq n_{\text{eval}}$), and the *training context length* n_{train} (the model’s training window). First, we evaluate the pretrained Qwen-7B-Chat at extrapolation lengths $n_{\text{eval}} > n_{\text{train}}$ ($n_{\text{train}} = 8192$ for Qwen-7B-Chat), sweeping the inverse-temperature exponent ξ_β in the length-dependent multiplier $\beta_n = c(\log n)^{\xi_\beta}$, applied per token, while dynamic-NTK RoPE (Appendix A.2) is held fixed (the RoPE base is rescaled per n_{eval}). The perplexity sweep, scored on the back half of each sliding window so that every scored token is conditioned on at least $n/2$ preceding tokens (formal definition in Appendix A.2), is reported per n_{eval} . On both PG-19 (PG19) (Rae et al., 2020) and Proof-Pile-2 (PP2) (Azerbayev et al., 2024), $\xi_\beta = 1$ is not a local minimum: the perplexity minima on the tested grid occur around $\xi_\beta^* \in [2, 2.5]$, near the $\xi_\beta = 2$ regime of YaRN (Peng et al., 2023). Qwen’s default $\log n$ scaling is therefore not optimal on the tested datasets and extrapolation lengths.

Second, the SSMAX design of Nakanishi (2025) was motivated by a probe experiment in which a learnable per-context-length inverse-temperature vector trained from scratch was fit well by $a_1 \log n + a_2$. We replay this probe on GPT-124M (Radford et al., 2019) trained from scratch with the nanoGPT codebase (Karpathy, 2022), with a length- $n_{\text{eval}} = 1024$ learnable vector β_n (one parameter per context position; protocol in Appendix B.1) but generalize the fit to $\beta_n = a_1(\log n)^{\xi_\beta}$ and sweep ξ_β . On both SlimPajama (SP) (Soboleva et al., 2023) and OpenWebText (OWT) (Gokaslan et al., 2019), across the reported training snapshots, the least-squares MSE for $n \geq 64$ has its minimum at $\xi_\beta^* \in \{0.40, 0.50\}$ across SlimPajama and OpenWebText; the SSMAX choice $\xi_\beta = 1$ is therefore not optimal even on its own motivating experiment.

Both sweeps therefore give concrete cases in which $\xi_\beta \neq 1$ is preferred (full protocols, grids, companion sweeps, and per-context numerics in Appendix B). They select different values of ξ_β , because perplexity and the learned β_n are different spatially-averaged observables of the same representation. Section 4 characterizes the general cause of softmax collapse: ξ_β is fixed by the row-wise N_n of attention scores.

4 Deterministic theory

The deterministic theory of softmax collapse is most naturally phrased in terms of how many competitors lie within a given gap of the winner, not in terms of which ordinal rank a competitor occupies: a one-step rank change can correspond to a negligible score change on one row and a large one on another, whereas increasing the gap by δ always suppresses a competitor’s weight by

the same factor $e^{-\beta\delta}$. Grouping the softmax partition function by gap rewrites it as a transform of a cumulative gap-counting curve, and the inverse temperature at which softmax collapses is then read off the exponential growth rate of that curve, namely the *upper-tail accumulation scale* Λ_n of [Section 4.2](#). [Section 4.1](#) first fixes the collapse observables against which Λ_n is identified as the relevant scale.

4.1 Collapse observables and the critical scale

Definition 4.1 (Collapse observables). Adopt the softmax probabilities $p_{n,j}(\beta)$ from [Section 2.1](#). The *Shannon entropy* is $H_n(\beta) := -\sum_{j=1}^n p_{n,j}(\beta) \log p_{n,j}(\beta)$, and the *top-two weight gap* $D_n(\beta)$ is the difference between the largest and second-largest entries of $(p_{n,j}(\beta))_{j=1}^n$. Along a positive deterministic sequence (β_n) , we say *top-two collapse* holds if $D_n(\beta_n) \rightarrow 0$, *entropy collapse* if $H_n(\beta_n) \rightarrow 0$, and *rank collapse* if $\max_{i,j} |p_{n,i}(\beta_n) - p_{n,j}(\beta_n)| \rightarrow 0$.

Definition 4.2 (Critical scale). A positive deterministic sequence (X_n) is a *rank-entropy scale* (RE scale) if, for every positive deterministic sequence (β_n) ,

$$\beta_n/X_n \rightarrow 0 \implies \text{rank collapse}, \quad \beta_n/X_n \rightarrow \infty \implies \text{entropy collapse},$$

in the sense of [Definition 4.1](#), and a *top-two-entropy scale* (TE scale) if the subcritical conclusion is replaced by top-two collapse. Each is unique up to \asymp when it exists.

We refer to TE and RE scales collectively as *critical scales*: each is a deterministic sequence that separates a subcritical regime, in which a collapse observable vanishes, from a supercritical regime in which entropy collapses. Rank collapse is the standard transformer-literature notion of convergence of an attention row toward the uniform law $(1/n, \dots, 1/n)$ ([Dong et al., 2021](#); [Noci et al., 2022](#); [Geshkovski et al., 2025](#)), strictly stronger than top-two collapse.

The primary scale here is Λ_n of [Section 4.2](#), which [Theorem 4.6](#) identifies as a critical scale (top-two/entropy sense of [Definition 4.2](#)) and which inverse-temperature calibration requires ([Corollary 4.8](#)). [Corollary 4.7](#) additionally upgrades Λ_n to the standard rank-collapse boundary under $C_n := \Lambda_n \Delta_n = \alpha_n \log n \rightarrow \infty$ ([Appendix D](#) for the contrary case), an observable-specific refinement that does not change the calibration principle.

4.2 Counting function, upper-tail accumulation scale, and contact point

Definition 4.3 (Cumulative gap-counting function). Set $z_n^* := \max_{1 \leq j \leq n} z_{n,j}$. The *cumulative gap-counting function*

$$N_n(t) := \#\{j \mid z_n^* - z_{n,j} \leq t\}, \quad t \geq 0,$$

counts the indices j with $z_n^* - z_{n,j} \leq t$; such an index j is called a *t-competitor* (the prefix t is dropped when unambiguous). In the physics analogy with $-z_{n,j}$ as energies, the gap $z_n^* - z_{n,j}$ is the excitation above the ground state $z = z_n^*$, and $N_n(t)$ counts states with excitation energy at most t .

The softmax probabilities of [Section 2.1](#) factor through the normalised partition function $Z_n(\beta) := \sum_{j=1}^n e^{-\beta(z_n^* - z_{n,j})}$, $p_{n,j}(\beta) = \exp[-\beta(z_n^* - z_{n,j})]/Z_n(\beta)$, and integration by parts (with $N_n(0^-) = 0$ and $e^{-\beta t} N_n(t) \rightarrow 0$ as $t \rightarrow \infty$) gives

$$Z_n(\beta) = \beta \int_0^\infty e^{-\beta t} N_n(t) dt. \quad (4.1)$$

The integrand of [\(4.1\)](#) is $e^{-\beta t} N_n(t)$. Whether the exponential damping $e^{-\beta t}$ outpaces the growth of $N_n(t)$ is captured by the envelope $N_n(t) \leq e^{\beta t}$, and the smallest exponent for which this envelope holds is the next definition.

Definition 4.4 (Upper-tail accumulation scale). The *upper-tail accumulation scale* Λ_n is the smallest exponent for which the envelope

$$N_n(t) \leq e^{\Lambda_n t} \quad (t > 0) \quad (4.2)$$

holds, equivalently

$$\Lambda_n := \sup_{t>0} \frac{\log N_n(t)}{t}. \quad (4.3)$$

Throughout the remainder of this section, we assume $\Lambda_n < +\infty$ eventually in n ; the boundary case $\Lambda_n = \infty$ (ties at the maximum, which forces $\log N_n(t)/t \rightarrow \infty$ as $t \downarrow 0$) is deferred to [Corollary C.2](#). Under this finite- Λ_n assumption the map $t \mapsto \log N_n(t)/t$ is non-increasing between consecutive competitor gaps and the supremum is attained as a maximum at some positive competitor gap $z_n^* - z_{n,j} > 0$ ([Lemma C.1](#)).

Definition 4.5 (Contact point). Call a positive competitor gap $u = z_n^* - z_{n,j} > 0$ a *contact gap* if $\log N_n(u)/u = \Lambda_n$ (the envelope $N \leq e^{\Lambda_n t}$ is attained at $t = u$). Let Δ_n be the largest such gap, and define the *contact accumulation exponent* $\alpha_n := \log N_n(\Delta_n)/\log n$. The pair (α_n, Δ_n) is the (largest) *contact point* and satisfies the *contact formula*

$$\Lambda_n = \frac{\alpha_n \log n}{\Delta_n}. \quad (4.4)$$

[Figure 2](#) shows the gap-counting curve, the exponential envelope, and the contact point. The coordinate α_n records the finite- n contact count on the scale of n , while Δ_n records the corresponding gap. The contact formula (4.4) is the only relation between these coordinates used below.

Theorem 4.6. (Λ_n) is the TE scale.

Proof. Set $s_n := \beta_n/\Lambda_n$.

Subcritical direction. Let $\eta_n > 0$ be the gap to the closest competitor, then $D_n(\beta) = (1 - e^{-\beta\eta_n})/Z_n(\beta)$. Suppose $s_n \rightarrow 0$. By (4.4), $N_n(\Delta_n) = n^{\alpha_n}$ and $\beta_n \Delta_n = s_n \alpha_n \log n$, so monotonicity of $e^{-\beta_n t}$ on the $N_n(\Delta_n)$ tokens with $z_n^* - z_{n,j} \leq \Delta_n$ gives

$$Z_n(\beta_n) \geq N_n(\Delta_n) e^{-\beta_n \Delta_n} = n^{\alpha_n(1-s_n)} \geq n^{\alpha_n/2}$$

for all large n since $s_n \leq 1/2$ eventually. Using $1 - e^{-\beta_n t} \leq \beta_n t$ and $\eta_n \leq \Delta_n$, it holds that $D_n(\beta_n) \leq \beta_n \eta_n / Z_n(\beta_n) \leq \beta_n \Delta_n / n^{\alpha_n/2} = s_n \alpha_n \log n / n^{\alpha_n/2} \leq (2/e) s_n \rightarrow 0$, where the last step uses $\sup_{a>0} a \log n / n^{a/2} = 2/e$.

Supercritical direction. $H_n(\beta_n) = \log Z_n(\beta_n) - \beta_n Z_n'(\beta_n) / Z_n(\beta_n)$. Suppose $s_n \rightarrow \infty$. The winner ($z_{n,j^*} = z_n^*$) contributes 1, so $Z_n(\beta_n) \geq 1$. The envelope (4.2) and the integral form (4.1) give

$$Z_n(\beta_n) \leq \beta_n \int_0^\infty e^{-(\beta_n - \Lambda_n)t} dt = \frac{\beta_n}{\beta_n - \Lambda_n}, \quad (4.5)$$

which $\rightarrow 1$, so $Z_n(\beta_n) \rightarrow 1$. Now, differentiating (4.1) gives $-\beta Z_n'(\beta) = \beta^2 \int_0^\infty t e^{-\beta t} N_n(t) dt - Z_n(\beta)$. Since $0 \leq -\beta Z_n'(\beta)$, $N_n(t) \leq e^{\Lambda_n t}$, and $Z_n(\beta) \geq 1$, we have $0 \leq -\beta Z_n'(\beta) \leq (\beta/(\beta - \Lambda_n))^2 - 1$ for $\beta > \Lambda_n$. At $\beta = \beta_n$ this is $o(1)$, so $H_n(\beta_n) \rightarrow 0$ follows from $Z_n(\beta_n) \rightarrow 1$. \square

Corollary 4.7. (Λ_n) is the RE scale if the contact-count entropy $C_n := \Lambda_n \Delta_n = \alpha_n \log n$ diverges.

A diverging contact-count entropy is what lets the rank-collapse argument absorb the lower-order tail of N_n and upgrade the TE scale to the RE scale (proof and the rank-resolved boundary in the contrary case in [Appendix D](#)).

4.3 Logarithmic critical-scaling exponent

Having established that Λ_n is a critical scale, we now record how its logarithmic growth rate is read from the contact coordinates of [Definition 4.5](#).

For any positive sequence (X_n) , if $X_n \asymp (\log n)^\xi$, then the exponent is unique when it exists: if ξ and ξ' both work, then $(\log n)^{\xi-\xi'}$ is bounded above and below, forcing $\xi = \xi'$. We call this ξ the *logarithmic growth exponent* of (X_n) and denote it ξ_X , so that

$$X_n \asymp (\log n)^{\xi_X}. \quad (4.6)$$

This single rule produces $\xi_\Lambda, \xi_\alpha, \xi_\Delta, \xi_\beta$ as instances of one family. The principal exponent of the system is ξ_Λ , the growth exponent of the upper-tail accumulation scale Λ_n .

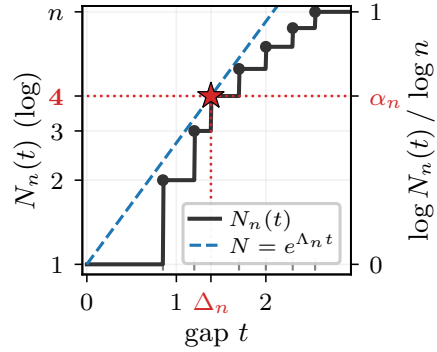


Figure 2: $N_n(t)$ and envelope $N = e^{\Lambda_n t}$; contact point (red star). Sorted-rank version: [Figure 6](#).

Corollary 4.8 (Exponent-selection rule). *Under $\Lambda_n \asymp (\log n)^{\xi_\Lambda}$ and $\beta_n \asymp (\log n)^{\xi_\beta}$, any schedule avoiding both top-two and entropy collapse has $\xi_\beta = \xi_\Lambda$ (otherwise $\beta_n/\Lambda_n \rightarrow 0$ or $\rightarrow \infty$, contradicting [Theorem 4.6](#)).*

The contact formula (4.4) expresses ξ_Λ in the contact coordinates of [Definition 4.5](#) as a linear combination.

Corollary 4.9 (Coordinate decomposition of ξ_Λ). *If any two of $\Lambda_n, \alpha_n, \Delta_n$ admit logarithmic growth exponents in the sense of (4.6), then so does the third, and they satisfy*

$$\xi_\Lambda = \xi_\alpha - \xi_\Delta + 1. \quad (4.7)$$

Proof. Multiplying \asymp -classes in the contact formula (4.4) gives $\Lambda_n = \alpha_n (\log n) \Delta_n^{-1} \asymp (\log n)^{\xi_\alpha} (\log n) (\log n)^{-\xi_\Delta} = (\log n)^{\xi_\alpha - \xi_\Delta + 1}$, and uniqueness of the exponent yields (4.7). Solving the contact formula for α_n or Δ_n covers the symmetric directions. \square

The corollary makes ξ_α, ξ_Δ first-class coordinate exponents on equal footing with ξ_Λ , and the side of 1 on which ξ_Λ lands is determined by the sign of $\xi_\alpha - \xi_\Delta$. [Section 4.5.2](#) uses this decomposition empirically.

4.4 Gap-counting on the equicorrelated configuration and a block extension

The contact formula (4.4) constrains the one-row N_n but not the configuration behind it. The deterministic equicorrelated (“simplex”) configuration of [Cowsik et al. \(2025\)](#), whose critical $\beta_n \asymp \log n$ was established by [Chen et al. \(2025\)](#), is the simplest configuration to which the framework applies; gap-counting reads ξ_Λ off it directly. A balanced block-constant extension also tunes the contact count α_n . Both body constructions take the score matrix as a symmetric Gram matrix Σ_n , equivalently the self-attention score matrix (2.1) with $W_n^Q = W_n^K$ ([Proposition C.4](#)); this $Q = K$ restriction is standard in theoretical analyses of attention ([Chen et al., 2025](#); [Geshkovski et al., 2023](#); [Arnaboldi et al., 2025](#)). [Chen et al. \(2025\)](#), in particular, work with the equicorrelated Gram of identity-coupled tokens, equivalent in our notation to the $W_n^Q = W_n^K = I$ specialization of (2.1). In both body constructions, $N_n(t)$ has at most two positive jumps. We write δ_n for the minimum positive gap and reserve Δ_n for the contact gap of [Definition 4.5](#); they coincide ($\Delta_n = \delta_n$) only in the within-block-dominant case.

Equicorrelated (simplex) configuration. With common norm $\|x_i\|^2 = q$ and pairwise inner product $\langle x_i, x_j \rangle = \rho < q$, set $J_n := \mathbf{1}\mathbf{1}^\top$, $r_n^2 := q$, $\Delta_n := q - \rho$ to obtain

$$\Sigma_n^{\text{simp}} := (r_n^2 - \Delta_n)J_n + \Delta_n I_n \geq 0.$$

Every query has flat competitor gap Δ_n , so N_n jumps from 1 to n at $t = \Delta_n$ and $\Lambda_n = \log n / \Delta_n$, $\alpha_n = 1$, the full-count endpoint. The $\beta_n \asymp \log n$ scaling of [Chen et al. \(2025\)](#) is the $\xi_\Lambda = 1$ slice ($\Delta_n = \Theta(1)$); $\Delta_n = (\log n)^{1 - \xi_\Lambda}$ realizes any $\xi_\Lambda \geq 0$. Reading off the contact coordinates gives $\xi_\alpha = 0$ and $\xi_\Delta = 1 - \xi_\Lambda$, which satisfy the decomposition (4.7) of [Corollary 4.9](#): this configuration sits on the $\xi_\alpha = 0$ axis with ξ_Λ entirely carried by ξ_Δ .

Two-level block-constant extension. A balanced block-constant analogue of Σ_n^{simp} tunes α_n as well as ξ_Λ . Fix $m_n \in \{2, \dots, n\}$ with $m_n \mid n$, and partition $\{1, \dots, n\}$ into blocks of size m_n . Let B_n be the block-membership matrix, equivalently the block-diagonal matrix with n/m_n diagonal blocks equal to J_{m_n} . For $0 < \delta_n < \tau_n \leq r_n^2$, define

$$\Sigma_n^{\text{block}} := \delta_n I_n + (\tau_n - \delta_n) B_n + (r_n^2 - \tau_n) J_n \geq 0. \quad (4.8)$$

Positivity follows from $I_n, B_n, J_n \geq 0$ and the nonnegative coefficients. The entries are r_n^2 on the diagonal, $r_n^2 - \delta_n$ inside a block, and $r_n^2 - \tau_n$ across blocks; thus r_n^2 is a common score shift, while δ_n and τ_n are the two relevant row gaps. Consequently $N_n(t) = 1$ for $0 \leq t < \delta_n$, $N_n(t) = m_n$ for $\delta_n \leq t < \tau_n$, and $N_n(t) = n$ for $t \geq \tau_n$ ([Figure 3](#)). Hence

$$\Lambda_n = \max \left\{ \frac{\log m_n}{\delta_n}, \frac{\log n}{\tau_n} \right\}. \quad (4.9)$$

The smaller-gap jump dominates when $\log m_n / \delta_n > \log n / \tau_n$; then $\Delta_n = \delta_n$ and $\alpha_n = \log m_n / \log n$. A prescribed $\Lambda_n = (\log n)^{\xi_\Lambda}$ is realized by taking $\delta_n = \log m_n / (\log n)^{\xi_\Lambda}$

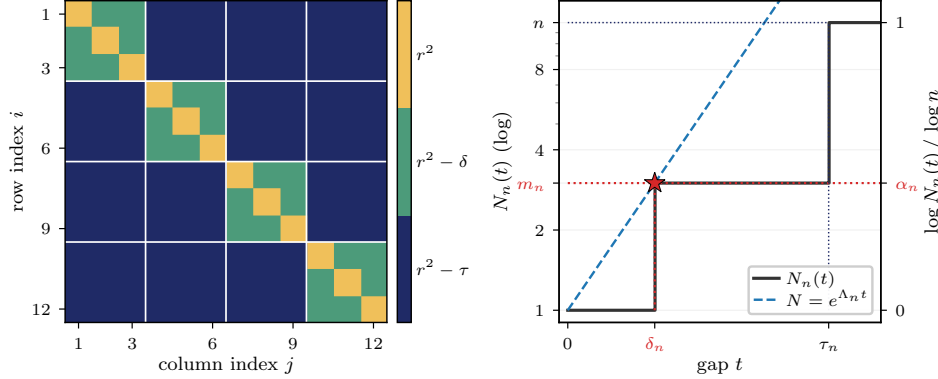


Figure 3: The two-level block-constant configuration reads Λ_n off the within-block gap δ_n in the dominant regime $\log m_n/\delta_n > \log n/\tau_n$. *Left*: the three-valued block-constant Gram matrix Σ_n^{block} (4.8) for $n = 12$, $m_n = 3$. *Right*: $N_n(t)$ jumps from 1 to m_n at $t = \delta_n$ and from m_n to n at $t = \tau_n$; the dashed envelope $N = e^{\Lambda_n t}$ is tangent at the contact point $(\Delta_n, N_n(\Delta_n)) = (\delta_n, m_n)$ (red star), with secondary axis $\log N_n(t)/\log n$.

and $\tau_n = C \log n / (\log n)^{\xi_\Lambda}$ with $C > 1$. With $m_n = n^\beta$ ($\beta \in (0, 1]$), the contact coordinates give $\xi_\alpha = 0$ and $\xi_\Delta = 1 - \xi_\Lambda$, recovering the simplex slice on a different $\alpha_n = \beta$ level. With bounded $m_n = m \geq 2$, $\alpha_n = \log m / \log n \asymp (\log n)^{-1}$ gives $\xi_\alpha = -1$, and $\delta_n = \log m / (\log n)^{\xi_\Lambda} \asymp (\log n)^{-\xi_\Lambda}$ gives $\xi_\Delta = -\xi_\Lambda$; both branches satisfy (4.7) (e.g. in the second branch $\xi_\alpha - \xi_\Delta + 1 = -1 - (-\xi_\Lambda) + 1 = \xi_\Lambda$). The block extension is the simplest configuration in which ξ_α takes values other than 0. The reverse case has $\Delta_n = \tau_n$ and $\alpha_n = 1$, coinciding with the simplex endpoint. When Λ_n is specified only up to \asymp , we pass to block-compatible subsequences with $m_n \mid n$.

The block-constant configuration corresponds to token vectors with a hierarchical cluster structure: within each block, tokens cluster around a common centroid at within-block gap δ_n , while distinct blocks are separated by the larger across-block gap τ_n . Such hierarchically structured token representations are themselves an object of study, with Li et al. (2023) giving a mechanistic account of topic clustering inside trained transformers and Garnier-Brun et al. (2025) analyzing attention block structure under hierarchical filtering of the input.

4.5 Empirical gap-counting analysis

We apply the gap-counting construction of Definitions 4.3 to 4.5 on two representative settings of Section 3: pretrained Qwen-7B-Chat at extrapolation context lengths (inference-time) and GPT-124M trained from scratch with a learnable per-position β_n vector (training-time). The aim is to read $\hat{\xi}_\Lambda$ from attention scores alone, align it with the ξ_β^* optima of Section 3, and verify the coordinate decomposition of Corollary 4.9 on real attention rows.

4.5.1 Aggregation protocol

Attention rows and exclusions. Each tuple (layer, head, document or validation batch, query position) determines an attention row: a length- n vector of scores $(z_{n,1}, \dots, z_{n,n})$. From every row, we read the contact triple $(\Lambda_n, \alpha_n, \Delta_n)$ via Definitions 4.3 to 4.5 at numerical tolerance $\epsilon = 10^{-6}$. Rows with $\log_{10} \Lambda_n > 5$ are exact-tie configurations ($N_n(0) \geq 2$) that saturate the floating-point supremum in (4.3); they are excluded from every aggregate below.

Cells and n -grids. Let \mathcal{C} index the experimental conditions: each cell $c \in \mathcal{C}$ is a fixed (setting, dataset, n_{eval}) on Qwen and a fixed (setting, dataset, training iteration) on nanoGPT. Each cell carries a finite n -grid $\mathcal{N}(c) \subset \mathbb{N}$, the set of context lengths at which scores are sampled in that cell (values listed in the next paragraph). For $c \in \mathcal{C}$ and $n \in \mathcal{N}(c)$, let $\mathcal{R}(c, n) := \{\text{non-tied attention rows of cell } c \text{ at context length } n\}$ and write $K(c, n) := |\mathcal{R}(c, n)|$ for its cardinality.

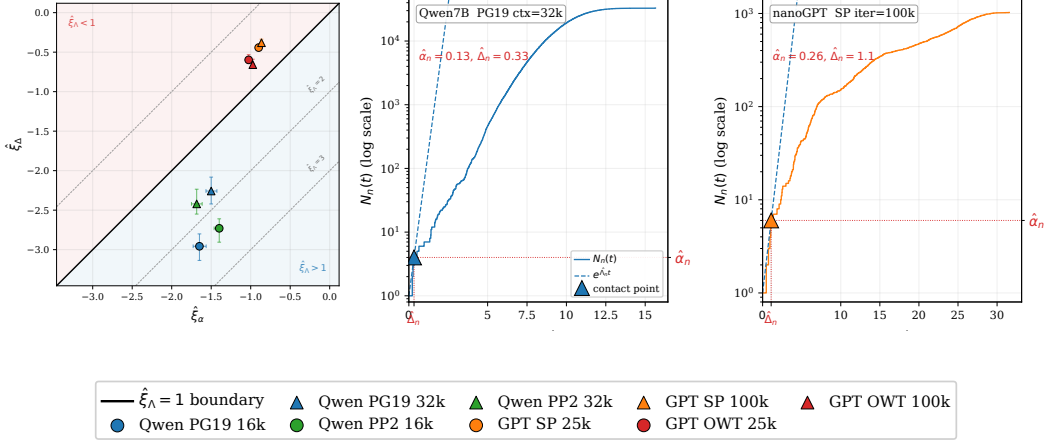


Figure 4: (Left) Qwen and nanoGPT cells land on opposite wedges of the $\hat{\xi}_\Lambda = 1$ boundary $\hat{\xi}_\alpha = \hat{\xi}_\Delta$, so the side of 1 each setting reaches is fixed by the sign of $\hat{\xi}_\alpha - \hat{\xi}_\Delta$ via (4.7). (Middle, right) The two sides recast as $N_n(t)$: Qwen’s contact lies near the origin on a steep Λ_n -envelope, nanoGPT’s further out on a shallow one.

Bucket-mean slope. For $X \in \{\Lambda, \alpha, \Delta\}$ and a row $i \in \mathcal{R}(c, n)$, write $X_n^{(i)}$ for the value of the contact-triple coordinate X read off row i at context length n . The *bucket mean* of $\log X_n$ in cell c at grid point $n \in \mathcal{N}(c)$ is $\overline{\log X}(c, n) := K(c, n)^{-1} \sum_{i \in \mathcal{R}(c, n)} \log X_n^{(i)}$. The estimator $\hat{\xi}_X(c)$ is the OLS slope of $\overline{\log X}(c, n)$ regressed on $\log \log n$ over $n \in \mathcal{N}(c)$; setting $X = \Lambda, \alpha, \Delta$ yields the three values $\hat{\xi}_\Lambda(c), \hat{\xi}_\alpha(c), \hat{\xi}_\Delta(c)$ reported in the body table.

Instantiation and intervals. We instantiate this on Qwen-7B-Chat over PG-19 (Rae et al., 2020) and Proof-Pile-2 (Azerbaiyev et al., 2024) at the two extrapolation context lengths $n_{\text{eval}} \in \{16384, 32768\}$ of Section 3 (4-point n -grid per n_{eval} , fit per- n_{eval} to keep the dynamic-NTK RoPE rescale fixed within a fit; full Qwen acquisition in Appendix G). On nanoGPT, GPT-124M is trained from scratch with a learnable per-position β_n at $n_{\text{eval}} = 1024$ (6-point grid $\{64, 128, 256, 512, 768, 1024\}$, three evaluation seeds pooled into $\mathcal{R}(c, n)$; configurations in Appendix A.3, checkpoint selection and the per-(layer, head) and rescaled-gap variants in Appendix F). Bracketed intervals in Table 2 (and tie %) are half the IQR of $B = 200$ bootstrap resamples over the cell’s natural unit set, (ℓ, h) on Qwen and (s, ℓ, h) on nanoGPT.

4.5.2 Comparing the gap-counting reading with the Section 3 sweeps

Cell-by-cell agreement. Table 2 aligns $\hat{\xi}_\Lambda$ with the Section 3 optimum ξ_β^* on eight (setting, run, iter) cells. On Qwen, the per- n_{eval} PPL optima $\xi_{\beta, \text{PPL}}^*$ and $\hat{\xi}_\Lambda$ agree within the §3 0.5-grid (absolute gap ≤ 0.26), with both decreasing from $\xi_\beta^* \in [2.31, 2.50]$ at $n_{\text{eval}} = 16384$ to $[1.74, 2.00]$ at $n_{\text{eval}} = 32768$. On nanoGPT, $\hat{\xi}_\Lambda$ matches the multiplier-side $\hat{\xi}_\beta$ on the same six-point domain to $|\hat{\xi}_\Lambda - \hat{\xi}_\beta| \in \{0.12, 0.14\}$ at iter = 25k and $\{0.17, 0.27\}$ at iter = 100k. The two columns are read off disjoint inputs (attention scores vs. the trained β_n vector); Theorem 4.6 predicts equality only asymptotically, consistent with the residual on the nanoGPT $n \leq 1024$ window.

Coordinate decomposition. The decomposition (4.7) of Corollary 4.9 carries through to the bucket-mean slopes, and the right two columns of Table 2 confirm $\hat{\xi}_\Lambda = \hat{\xi}_\alpha - \hat{\xi}_\Delta + 1$ row by row at the table’s precision; the side of 1 on which $\hat{\xi}_\Lambda$ lands is fixed by the sign of $\hat{\xi}_\alpha - \hat{\xi}_\Delta$. Figure 4 (left) plots the eight $(\hat{\xi}_\alpha, \hat{\xi}_\Delta)$ pairs of Table 2: the four Qwen extrapolation-time points sit below the diagonal $\hat{\xi}_\alpha = \hat{\xi}_\Delta$ ($|\hat{\xi}_\Delta| > |\hat{\xi}_\alpha|$, contact gap shrinks faster with $\log \log n$), and the four nanoGPT training-time points sit above it ($|\hat{\xi}_\alpha| > |\hat{\xi}_\Delta|$, contact count shrinks faster). The middle and right panels recast one representative row per contrast cell (Qwen PG-19 $n_{\text{eval}} = 32768$ at $n = 32768$; nanoGPT SlimPajama iter = 100k at $n = 1024$) as $N_n(t)$.

setting	dataset	$n_{\text{eval}}/\text{iter}$	tie %	ξ_{β}^* (Section 3)	$\hat{\xi}_{\Lambda}$	$\hat{\xi}_{\alpha}$	$\hat{\xi}_{\Delta}$
Qwen7B	PG19	16384	7.4 (± 0.2)	2.5	2.31 (± 0.10)	-1.65 (± 0.08)	-2.96 (± 0.17)
Qwen7B	PG19	32768	8.8 (± 0.2)	2.0	1.76 (± 0.10)	-1.50 (± 0.07)	-2.26 (± 0.17)
Qwen7B	PP2	16384	6.8 (± 0.2)	2.5	2.33 (± 0.11)	-1.40 (± 0.05)	-2.73 (± 0.15)
Qwen7B	PP2	32768	7.2 (± 0.2)	2.0	1.74 (± 0.11)	-1.68 (± 0.07)	-2.42 (± 0.16)
nanoGPT	SP	25k	2.8 (± 0.1)	0.40 (± 0.03)	0.54 (± 0.03)	-0.90 (± 0.01)	-0.44 (± 0.04)
nanoGPT	SP	100k	6.0 (± 0.4)	0.35 (± 0.04)	0.52 (± 0.03)	-0.86 (± 0.01)	-0.38 (± 0.04)
nanoGPT	OWT	25k	4.0 (± 0.4)	0.46 (± 0.05)	0.57 (± 0.04)	-1.03 (± 0.02)	-0.60 (± 0.05)
nanoGPT	OWT	100k	5.7 (± 0.3)	0.42 (± 0.05)	0.69 (± 0.05)	-0.97 (± 0.02)	-0.66 (± 0.05)

Table 2: $\hat{\xi}_{\Lambda}$, read off attention scores alone, lands on the same side of $\xi = 1$ as the sweep optimum ξ_{β}^* in every cell: both exceed 1 on the four Qwen cells, both fall below 1 on the four nanoGPT cells.

Each $\hat{\xi}_X$ ($X \in \{\Lambda, \alpha, \Delta\}$) is the OLS slope of the bucket-mean $\overline{\log X}(c, n)$ regressed on $\log \log n$ across the cell’s n -grid (Section 4.5.1); ξ_{β}^* is the per-cell optimum from Section 3. Bracketed intervals are half-IQRs of $B = 200$ bootstrap resamples over (ℓ, h) on Qwen and (s, ℓ, h) on nanoGPT, with the same convention for tie %, the fraction of exact-tie rows ($N_n(0) \geq 2$, excluded from aggregates).

Calibration character of Λ_n . Table 2 evaluates Λ_n as a calibration scale for inverse temperature: agreement with ξ_{β}^* relies only on Corollary 4.8 and does not require TE and RE scales to coincide. The rank-side checks in Appendix D.1 are a sanity check that the stronger coordinate-wise observable is not pathological (Corollary 4.7 on the four nanoGPT cells; the rank-resolved substitute and a direct p_n^* sweep on the four Qwen cells with bounded C_n).

5 Discussion and Conclusion

This paper asks what determines the critical scaling of inverse temperature for self-attention in the long-context limit. Our answer is that it is determined by $(\Lambda_n, \alpha_n, \Delta_n)$. The cumulative gap-counting function $N_n(t)$ of Definition 4.3 records how many competitors lie within each gap of the winning score, and the upper-tail accumulation scale Λ_n of Definition 4.4 gives the relevant scale. Theorem 4.6 identifies Λ_n as a critical scale for arbitrary deterministic score rows; Corollary 4.7 sharpens this to the standard rank-collapse boundary whenever the contact-count entropy $\alpha_n \log n = \Lambda_n \Delta_n$ diverges, with empirical verification on the bounded- C_n cells via Appendix D.1. Thus the exponent ξ_{β} in $\beta_n \asymp (\log n)^{\xi_{\beta}}$ is not universal: any non-degenerate schedule has $\xi_{\beta} = \xi_{\Lambda}$ (Corollary 4.8), the logarithmic growth rate of Λ_n in the sense of (4.6). Equivalently, the contact formula (4.4) shows that ξ_{β} is determined by both the contact count α_n and the contact gap Δ_n of Definition 4.5, namely $\xi_{\beta} = \xi_{\alpha} - \xi_{\Delta} + 1$ (Corollary 4.9). This also explains why the mechanisms in Table 1 give different exponents (they induce different N_n , not different universal laws), and why empirical long-context behavior can prefer values away from the legacy logarithmic choice $\xi_{\beta} = 1$.

Limitations and open problem. The main limitation of the present framework is that the score family, and hence $(\Lambda_n, \alpha_n, \Delta_n)$, is taken as given. We do not yet derive it from the architecture, positional encoding, data distribution, or training dynamics of a concrete transformer. A natural open problem is therefore to endogenize these quantities through the dynamics of self-attention. Recent inference-time theories of recurrent or infinitely deep self-attention describe token representations as interacting particles whose empirical geometry can develop clustered, metastable, or lower-dimensional structure across depth or loop time (Geshkovski et al., 2023, 2024; Karagodin et al., 2024; Bruno et al., 2025; Tomihari and Karakida, 2025; Rigollet, 2026). Complementary learning-time analyses show that training can progressively encode semantic, positional, or hierarchical structure into embeddings and attention maps (Li et al., 2023; Garnier-Brun et al., 2025; Arnaboldi et al., 2025). Coupling such inference-time and learning-time dynamics with the present gap-counting theory would turn $N_n(t)$, Λ_n , and (α_n, Δ_n) into observables that depend on depth, loop time, and training time, making it possible to predict how the critical inverse-temperature scale is shaped by the model and data rather than treating the score family as fixed.

Acknowledgments

T.H. was supported by JST BOOST Grant Number JPMJBY24G4. The authors are grateful to Ken M. Nakanishi for sharing details of the experimental setup for SSMax.

References

- Ashish Vaswani, Noam Shazeer, Niki Parmar, Jakob Uszkoreit, Llion Jones, Aidan N Gomez, Łukasz Kaiser, and Illia Polosukhin. Attention is all you need. *Advances in neural information processing systems*, 30, 2017.
- Jiri Hron, Yasaman Bahri, Jascha Sohl-Dickstein, and Roman Novak. Infinite attention: NNGP and NTK for deep attention networks. In *International Conference on Machine Learning (ICML)*, pages 4376–4386. PMLR, 2020.
- Blake Bordelon, Hamza Chaudhry, and Cengiz Pehlevan. Infinite limits of multi-head transformer dynamics. *Advances in Neural Information Processing Systems*, 37:35824–35878, 2024.
- Mana Sakai, Ryo Karakida, and Masaaki Imaizumi. Infinite-width limit of a single attention layer: Analysis via tensor programs. In *Advances in Neural Information Processing Systems (NeurIPS)*, 2025, [arXiv:2506.00846](https://arxiv.org/abs/2506.00846). URL <https://arxiv.org/abs/2506.00846>.
- Borjan Geshkovski, Cyril Letrouit, Yury Polyanskiy, and Philippe Rigollet. A mathematical perspective on Transformers. *Bulletin of the American Mathematical Society*, 62(3):427–479, 2025. Also [arXiv:2312.10794](https://arxiv.org/abs/2312.10794).
- Giuseppe Bruno, Federico Pasqualotto, and Andrea Agazzi. A multiscale analysis of mean-field transformers in the moderate interaction regime. In *Advances in Neural Information Processing Systems (NeurIPS)*, 2025, [arXiv:2509.25040](https://arxiv.org/abs/2509.25040). URL <https://arxiv.org/abs/2509.25040>. Oral.
- Thiziri Nait Saada, Alireza Naderi, and Jared Tanner. Mind the gap: a spectral analysis of rank collapse and signal propagation in attention layers. In *Forty-second International Conference on Machine Learning*, 2025.
- Alessio Giorlandino and Sebastian Goldt. Two failure modes of deep transformers and how to avoid them: a unified theory of signal propagation at initialisation. In *International Conference on Learning Representations*, 2026, [arXiv:2505.24333](https://arxiv.org/abs/2505.24333). URL <https://arxiv.org/abs/2505.24333>.
- Shi Chen, Zhengqiang Lin, Yury Polyanskiy, and Philippe Rigollet. Critical attention scaling in long-context transformers. *arXiv preprint*, 2025, [arXiv:2510.05554](https://arxiv.org/abs/2510.05554). URL <https://arxiv.org/abs/2510.05554>.
- Jinze Bai, Shuai Bai, Yunfei Chu, Zeyu Cui, Kai Dang, Xiaodong Deng, Yang Fan, Wenbin Ge, Yu Han, Fei Huang, Binyuan Hui, Luo Ji, Mei Li, Junyang Lin, Runji Lin, Dayiheng Liu, Gao Liu, Chengqiang Lu, Keming Lu, Jianxin Ma, Rui Men, Xingzhang Ren, Xuancheng Ren, Chuanqi Tan, Sinan Tan, Jianhong Tu, Peng Wang, Shijie Wang, Wei Wang, Shengguang Wu, Benfeng Xu, Jin Xu, An Yang, Hao Yang, Jian Yang, Shusheng Yang, Yang Yao, Bowen Yu, Hongyi Yuan, Zheng Yuan, Jianwei Zhang, Xingxuan Zhang, Yichang Zhang, Zhenru Zhang, Chang Zhou, Jingren Zhou, Xiaohuan Zhou, and Tianhang Zhu. Qwen technical report. *arXiv preprint*, 2023, [arXiv:2309.16609](https://arxiv.org/abs/2309.16609). URL <https://arxiv.org/abs/2309.16609>.
- Ken M Nakanishi. Scalable-softmax is superior for attention. *arXiv preprint*, 2025, [arXiv:2501.19399](https://arxiv.org/abs/2501.19399). URL <https://arxiv.org/abs/2501.19399>.
- Bowen Peng, Jeffrey Quesnelle, Honglu Fan, and Enrico Shippole. YaRN: Efficient context window extension of large language models. *arXiv preprint*, 2023, [arXiv:2309.00071](https://arxiv.org/abs/2309.00071). URL <https://arxiv.org/abs/2309.00071>. Published at ICLR 2024.
- Ben Anson, Xi Wang, and Laurence Aitchison. Scale-invariant attention. In *Advances in Neural Information Processing Systems (NeurIPS)*, 2025, [arXiv:2505.17083](https://arxiv.org/abs/2505.17083). URL <https://arxiv.org/abs/2505.17083>.

- B. Derrida. Random-energy model: An exactly solvable model of disordered systems. *Physical Review B*, 24(5):2613–2626, 1981.
- Jack W. Rae, Anna Potapenko, Siddhant M. Jayakumar, Chloe Hillier, and Timothy P. Lillicrap. Compressive transformers for long-range sequence modelling. In *International Conference on Learning Representations*, 2020, arXiv:1911.05507. URL <https://openreview.net/forum?id=SylKikSYDH>.
- Zhangir Azerbayev, Hailey Schoelkopf, Keiran Paster, Marco Dos Santos, Stephen McAleer, Albert Q. Jiang, Jia Deng, Stella Biderman, and Sean Welleck. Llemma: An open language model for mathematics. In *International Conference on Learning Representations*, 2024, arXiv:2310.10631. URL <https://openreview.net/forum?id=4WnqRR915j>.
- Alec Radford, Jeff Wu, Rewon Child, David Luan, Dario Amodei, and Ilya Sutskever. Language models are unsupervised multitask learners. Technical report, OpenAI, 2019. URL https://cdn.openai.com/better-language-models/language_models_are_unsupervised_multitask_learners.pdf.
- Andrej Karpathy. nanoGPT: The simplest, fastest repository for training/finetuning medium-sized GPTs. <https://github.com/karpathy/nanoGPT>, 2022.
- Daria Soboleva, Faisal Al-Khateeb, Robert Myers, Jacob R. Steeves, Joel Hestness, and Nolan Dey. SlimPajama: A 627B token cleaned and deduplicated version of RedPajama. <https://cerebras.ai/blog/slimpajama-a-627b-token-cleaned-and-deduplicated-version-of-redpajama>, 2023.
- Aaron Gokaslan, Vanya Cohen, Ellie Pavlick, and Stefanie Tellex. OpenWebText corpus. <http://Skylion007.github.io/OpenWebTextCorpus>, 2019.
- Yihe Dong, Jean-Baptiste Cordonnier, and Andreas Loukas. Attention is not all you need: pure attention loses rank doubly exponentially with depth. In *International Conference on Machine Learning (ICML)*, volume 139 of *Proceedings of Machine Learning Research*, pages 2793–2803, 2021.
- Lorenzo Noci, Sotiris Anagnostidis, Luca Biggio, Antonio Orvieto, Sidak Pal Singh, and Aurelien Lucchi. Signal propagation in Transformers: Theoretical perspectives and the role of rank collapse. In *Advances in Neural Information Processing Systems (NeurIPS)*, 2022, arXiv:2206.03126.
- Aditya Cowsik, Tamra Nebabu, Xiao-Liang Qi, and Surya Ganguli. Geometric dynamics of signal propagation predict trainability of transformers. *Physical Review E*, 112:055301, 2025. Also arXiv:2403.02579.
- Borjan Geshkovski, Cyril Letrouit, Yury Polyanskiy, and Philippe Rigollet. The emergence of clusters in self-attention dynamics. In *Advances in Neural Information Processing Systems (NeurIPS)*, 2023, arXiv:2305.05465.
- Luca Arnaboldi, Bruno Loureiro, Ludovic Stephan, Florent Krzakala, and Lenka Zdeborová. Asymptotics of SGD in sequence-single index models and single-layer attention networks. In *Advances in Neural Information Processing Systems (NeurIPS)*, 2025, arXiv:2506.02651. URL <https://arxiv.org/abs/2506.02651>.
- Yuchen Li, Yuanzhi Li, and Andrej Risteski. How do transformers learn topic structure: Towards a mechanistic understanding. In *Proceedings of the 40th International Conference on Machine Learning (ICML)*, volume 202 of *Proceedings of Machine Learning Research*, pages 19689–19729, 2023. URL <https://proceedings.mlr.press/v202/li23p.html>.
- Jérôme Garnier-Brun, Marc Mézard, Emanuele Moscato, and Luca Saglietti. How transformers learn structured data: Insights from hierarchical filtering. In *Proceedings of the 42nd International Conference on Machine Learning (ICML)*, 2025. URL <https://openreview.net/forum?id=AVXApuBCvN>.

- Borjan Geshkovski, Hugo Koubbi, Yury Polyanskiy, and Philippe Rigollet. Dynamic metastability in the self-attention model. *arXiv preprint arXiv:2410.06833*, 2024, [arXiv:2410.06833](https://arxiv.org/abs/2410.06833). URL <https://arxiv.org/abs/2410.06833>.
- Nikita Karagodin, Yury Polyanskiy, and Philippe Rigollet. Clustering in causal attention masking. In *Advances in Neural Information Processing Systems (NeurIPS)*, volume 37, pages 115652–115681, 2024, [arXiv:2411.04990](https://proceedings.neurips.cc/paper_files/paper/2024/hash/d18d208fa9c333483e5724ade7bfff0f-Abstract-Conference.html). URL https://proceedings.neurips.cc/paper_files/paper/2024/hash/d18d208fa9c333483e5724ade7bfff0f-Abstract-Conference.html.
- Akiyoshi Tomihari and Ryo Karakida. Recurrent self-attention dynamics: An energy-agnostic perspective from jacobians. In *Advances in Neural Information Processing Systems (NeurIPS)*, 2025, [arXiv:2505.19458](https://openreview.net/forum?id=GKLePUzy08). URL <https://openreview.net/forum?id=GKLePUzy08>.
- Philippe Rigollet. The mean-field dynamics of transformers. *arXiv preprint arXiv:2512.01868*, 2026, [arXiv:2512.01868](https://arxiv.org/abs/2512.01868). URL <https://arxiv.org/abs/2512.01868>. To appear in Proceedings of the ICM 2026.
- Jianlin Su, Murtadha Ahmed, Yu Lu, Shengfeng Pan, Wen Bo, and Yunfeng Liu. RoFormer: Enhanced transformer with rotary position embedding. *Neurocomputing*, 568:127063, 2024, [arXiv:2104.09864](https://arxiv.org/abs/2104.09864).

A Experimental setup

This appendix collects the experimental basic setup shared across the inference-time ξ -sweep of Section 3 and the training-time gap-exponent trajectory of Section 4.5.1. The per-experiment grids, seeds, ξ_0 values, and numerical tolerances are recorded in the corresponding protocol appendices (Appendices B, F and G.1).

A.1 Datasets

The Qwen long-context ξ -sweep (Section 3) draws documents from the PG-19 (Rae et al., 2020) test split and the Proof-Pile-2 (Azerbayev et al., 2024) arXiv test split (up to 20 per dataset per n_{eval} ; the per-cell counts entering the perplexity averages are listed in Appendix B.2). The Qwen-7B-Chat gap-counting analysis (Section 4.5) uses a smaller fixed subset of these documents because the per-row analysis is heavier: 4 from PG-19 and 5 from Proof-Pile-2 enter the headline statistics of Table 2, which together with the $(\xi_0, n_{\text{eval}}, \text{ratio})$ grid produces the 774,144 attention rows enumerated in Appendix G. The GPT-124M training-time runs of Sections 3 and 4.5.1 are pretrained on SlimPajama (Soboleva et al., 2023) and OpenWebText (Gokaslan et al., 2019), one run per dataset.

A.2 Qwen long-context evaluation

We probe two pretrained checkpoints: Qwen-1.8B-Chat with training window $n_{\text{train}} = 8192$, and Qwen-7B-Chat (32 transformer layers, 32 attention heads per layer) also with $n_{\text{train}} = 8192$. Both keep rotary position embeddings (Su et al., 2024) on with the dynamic-NTK RoPE base schedule of Peng et al. (2023, §3.4) defined just below. On top of dynamic-NTK, we apply the legacy length-dependent multiplier

$$m(n; \xi) = (\max(1, \log n / \log n_{\text{train}}))^\xi$$

to the attention logits at extrapolation lengths $n > n_{\text{train}}$, equivalent to the parameterization $\beta_n \propto (\log n)^\xi$ for $n > n_{\text{train}}$ and to the no-multiplier baseline at $\xi = 0$; the YaRN inverse-temperature window $\xi = 2$ (Peng et al., 2023) corresponds to the YaRN schedule as derived in Appendix E. The contexts n and ξ -grids vary by experiment and are recorded with the respective figures.

Dynamic-NTK RoPE. Standard RoPE (Su et al., 2024) rotates the per-head query/key pair in \mathbb{R}^d using a fixed base θ_0 (typically $\theta_0 = 10000$): the k -th coordinate pair at position i is multiplied by $R(i\theta_0^{-2k/d})$. The *dynamic-NTK* schedule of Peng et al. (2023, §3.4) (also Bai et al. 2023 for Qwen) replaces θ_0 by a per-evaluation base $\theta_0 s(n_{\text{eval}})$ where, with the extrapolation ratio $\rho(n_{\text{eval}}) := \max(1, n_{\text{eval}}/n_{\text{train}})$,

$$s(n_{\text{eval}}) := \rho(n_{\text{eval}})^{d/(d-2)}.$$

The base is recomputed once per inference window of size n_{eval} and then held fixed across positions $i \leq n_{\text{eval}}$ inside the window. The high-frequency rotations are nearly unchanged while the low-frequency ones are stretched, so embeddings of relative offsets that exceed n_{train} at evaluation time stay within the angular range the model saw during training. Throughout this paper, “dynamic-NTK RoPE” refers to this schedule, with the legacy multiplier $m(n; \xi)$ above applied as a separate inverse-temperature scalar on the attention logits.

Sliding-window perplexity. We report *back-half sliding-window perplexity*: a long document is partitioned into non-overlapping windows of length n_{eval} , and within each window only the second half (positions $j \in (n_{\text{eval}}/2, n_{\text{eval}}]$) contributes to the loss, so every scored token is conditioned on $\geq n_{\text{eval}}/2$ preceding tokens. Concretely, with $\ell(j)$ the cross-entropy of the model on the j -th token of the window, the window contribution to log-perplexity is $\sum_{j > n_{\text{eval}}/2} \ell(j) / (n_{\text{eval}}/2)$, averaged across windows and documents and exponentiated. This is the protocol called *strict sliding-window perplexity* in earlier drafts and in some external references; we drop the modifier in the body since the back-half restriction is the only convention used. The convention controls position-context confounding at extrapolation lengths $n_{\text{eval}} > n_{\text{train}}$: under no-overlap windows the early positions of a window see only short prefixes, which would otherwise dominate the loss for $n > n_{\text{train}}$.

A.3 GPT-124M training-time setup

GPT-124M (Radford et al., 2019) (12 transformer layers, 12 attention heads per layer, context length $n_{\text{eval}} = 1024$) is trained from scratch using the nanoGPT codebase (Karpathy, 2022) in four configurations: two positional encodings (learned absolute, as in GPT-2 (Radford et al., 2019); rotary (Su et al., 2024)) \times two pretraining datasets (SlimPajama, OpenWebText). Each configuration runs for 100,000 iterations with checkpoints saved every 5000 iterations; the seven milestones $\text{iter} \in \{0, 5\text{k}, 10\text{k}, 25\text{k}, 50\text{k}, 75\text{k}, 100\text{k}\}$ are the snapshots used by the body and appendix figures.

Learnable inverse-temperature vector β_n . Each model carries an additional length- n_{eval} vector β_n (one parameter per context position n) tied across layers and heads; per (layer, head) the actual attention multiplier is

$$\beta_{n,\ell,h} = s_{\ell,h} \beta_n + b_{\ell,h}, \tag{A.1}$$

with per-head scale $s_{\ell,h}$ and bias $b_{\ell,h}$ trained alongside β_n . The n -dependence is carried entirely by β_n ; the body’s β_n regression fit (Section 3) reads β_n off after training and fits it to $a_1 (\log n)^\xi$, while the gap-exponent diagnostic (Section 4.5.1) compares raw and effective gap exponents row-wise. Unlike SSMaX, which fixes $\beta_{n,\ell,h} = s_{\ell,h} \log n$ with a single scalar $s_{\ell,h}$ per head, here β_n is unconstrained at initialization and is shaped only by the training loss. The original SSMaX design-rationale experiment of Nakanishi (2025) used the same unconstrained β_n vector and fit it by least squares to $a_1 \log n + a_2$, motivating the logarithmic constraint.

Hyperparameters. Table 3 records the architecture, β_n realization, and optimization settings shared across the four configurations, together with the four (positional encoding, dataset) pairs that distinguish them. All values are read from the training configs of the runs (n_layer, n_head, n_embd, optimizer schedule, etc.).

A.4 Compute resources

All experiments ran on academic GPU clusters equipped with NVIDIA H100 GPUs (96 GB HBM3). Two job sizes were used: a single-GPU job (one H100) and a full-node job (eight H100s).

Qwen inference (Section 4.5 and Appendix A.2). The Qwen long-context ξ_β sweep (Section 3 and Figures 1a and 1b) and the gap-counting attention-row capture (Section 4.5.1) each run as single-GPU jobs. Per back-half sliding-window perplexity job (one (ξ_β , dataset) covering all five contexts $n_{\text{eval}} \in \{8192, 12288, 16384, 24576, 32768\}$ on 20 documents): ~ 25 minutes wall on one H100, of which ~ 5 minutes per context. Per attention-row gap capture job (one (ξ_0 , dataset, n_{eval} , doc)): ~ 2 minutes wall on one H100. The full ξ_β refinement to 0.1 resolution on Qwen-7B-Chat used ≤ 60 GPU-hours. The gap-counting capture for the body Table 2 cells, the ξ_0 -sweep, and the ξ_0 fixed-point refinement together used ~ 10 additional GPU-hours on the same single-H100 budget. Total Qwen H100-hours for the content reported in this paper: ~ 80 .

nanoGPT training-time runs (Appendices A.3 and F). Each of the four training-time GPT-124M runs of Table 3 runs as a full-node job (8 H100, distributed via torchrun with effective batch 2048 sequences of length 1024, walltime budget 24 hours per run). A complete run reaches 100,000 iterations in well under the budget; total nanoGPT training compute reported in this paper is bounded by 4 runs \times 24 h \times 8 H100 = 768 H100-hours. Per-checkpoint dump and post-processing for the seven milestone checkpoints $\{0, 5\text{k}, \dots, 100\text{k}\}$ on three evaluation seeds adds order 20 GPU-hours.

Storage. The Qwen full-gap safetensors at the body’s ($ds, n_{\text{eval}}, \xi_0, \text{doc}$) grid plus the off-grid points generated for the ξ_0 fixed-point search occupy ~ 150 GB of project-area storage; the nanoGPT checkpoint set occupies ~ 30 GB per training run.

Preliminary work. The headline compute above does not include preliminary ξ_β -sweep iterations on Qwen-1.8B-Chat at intermediate grid resolutions, exploratory ξ_0 ablations, and discarded gap-capture pipelines (direct top- k vs full sorted-gap dumps). Counting these, the full research project consumed roughly twice the headline budget, all on the same internal H100 clusters.

A.5 Reproducibility capsule

This subsection collects the environment and artifact pointers needed to reproduce the headline experiments alongside the protocols documented in Appendices A.2, A.3, B.2, F and G.

<i>Architecture (4 runs shared, GPT-2 124M)</i>	
Layers L	12
Attention heads H	12
Embedding dim d_{model}	768
Per-head dim $d_{qk} = d_v$	64
FFN dim d_{ff}	3072 ($= 4 d_{\text{model}}$)
Vocabulary size	50,257 (GPT-2 BPE; padded to 50,304)
Context length n_{eval}	1024
Linear bias	enabled
Dropout	0
Total parameters	$\sim 124\text{M}$
<i>Inverse-temperature β_n realization</i>	
Per-position factor β_n	learnable vector of length n_{eval} , init. $\beta_n[n] = 1$
Per-(layer,head) realization	$\beta_{n,\ell,h} = s_{\ell,h} \beta_n + b_{\ell,h}$ (Equation (A.1))
$s_{\ell,h}, b_{\ell,h}$	per-head, learnable; $s_{\ell,h}$ init. 1, $b_{\ell,h}$ init. 0
<i>Optimization (4 runs shared)</i>	
Optimizer	AdamW
Learning-rate schedule	cosine: $6 \times 10^{-4} \rightarrow 6 \times 10^{-5}$
Warmup	1000 iters
Weight decay	0.1
(β_1, β_2)	(0.9, 0.95)
Gradient clip	1.0
Per-step batch	32 sequences \times grad-accum 64 (effective 2048)
Precision	bfloat16
Iterations	100,000
Checkpoint cadence	every 5000 iters (milestone keep)
<i>Configurations (4 runs)</i>	
1: learned absolute PE	SlimPajama
2: learned absolute PE	OpenWebText
3: RoPE ($\theta_0 = 10000$)	SlimPajama
4: RoPE	OpenWebText

Table 3: GPT-124M training-time configuration. The four runs share the architecture, β_n realization, and optimization settings listed above; they differ only in the positional encoding (learned absolute as in Radford et al. 2019, or RoPE Su et al., 2024) and the pretraining dataset (SlimPajama Soboleva et al., 2023, or OpenWebText Gokaslan et al., 2019). Three evaluation seeds {1337, 1338, 1339} produce independent validation batches at every checkpoint.

Environment. We list only the dependencies that affect the experiment outputs; the SciPy-stack analysis packages used downstream of the captured CSVs are omitted because any current version reproduces the same numerics. The Qwen long-context evaluations run under Python 3.11 with PyTorch 2.6 (CUDA 12.4 build), transformers 4.32.0 (the version pinned by the Qwen-7B-Chat model card and required by the bundled custom modeling file loaded with trust_remote_code=True), flash-attn 2.8.3, and einops 0.8 (used inside that modeling file). The GPT-124M training-time runs use Python 3.12 with the same PyTorch build and tiktoken 0.12 (GPT-2 BPE). All experiments run on NVIDIA H100 (96 GB HBM3) GPUs.

Artifact identifiers. The Qwen checkpoints are the public Qwen/Qwen-7B-Chat and Qwen/Qwen-1.8B-Chat HuggingFace releases used as published (no fine-tuning); their bundled config.json reports transformers_version 4.32.0, fixing the modeling-file revision the trust_remote_code loader executes. The training-time runs are built on the public nanoGPT codebase (Karpathy, 2022) (snapshot from spring 2026) with the length- n_{eval} learnable β_n vector inserted as in (A.1). The text corpora are the deepmind/pg19, EleutherAI/proof-pile-2 (arXiv subset), cerebras/SlimPajama-627B, and SkyLion007/openwebtext HuggingFace dataset releases as of the experiment dates; tokenization uses each model’s bundled tokenizer (Qwen’s BPE for the Qwen evaluations, GPT-2 BPE via tiktoken for the nanoGPT training and validation passes).

Modification surface. The Qwen-side per-token multiplier $m(n; \xi) = (\max(1, \log n / \log n_{\text{train}}))^\xi$ of Appendix A.2 is applied after the per-head dot-product score $z_{n,j} = \langle \mathbf{q}_{n,i_n}, \mathbf{k}_{n,j} \rangle / \sqrt{d_{qk}}$ and before the softmax inside the modified Qwen forward pass; the unrescaled $z_{n,j}$ that the gap-counting analysis reads is the score before this multiplier and softmax are applied. Dynamic-NTK RoPE is the upstream Qwen schedule with the per- n_{eval} base rescale of Peng et al. (2023, §3.4), controlled by Qwen’s existing `use_dynamic_ntk` configuration switch. The nanoGPT-side modification is a single length- n_{eval} per-position scalar vector β_n initialised to one and trained jointly with the rest of the model; the per-(layer, head) affine $\beta_{n,\ell,h} = s_{\ell,h}\beta_n + b_{\ell,h}$ then folds into the attention computation as in (A.1).

Procedure cross-references. Document selection, query-position rule, bucket and n -grid choices, and bootstrap procedures are documented in the sections referenced above; the per-row attention-score acquisition pipeline is in Appendix G, and the reported \pm half-widths are derived as in Appendix B.2.

B Detailed protocols and aggregate numerics for the ξ_β -sweeps

This appendix records the body β_n regression-fit protocol and the training-time trajectory deferred from Section 3.

B.1 Learnable inverse-temperature vector: β_n regression-fit protocol and trajectory

The four-configuration training schedule and the per-(layer, head) realization (A.1) of the learnable vector β_n are as in Appendix A.3. At each of the seven milestone checkpoints, we extract β_n (a length-1024 vector) and fit the bias-free regression model $\beta_n = a_1(\log n)^{\xi_\beta}$ in two settings:

	Domain	Bias a_2	ξ_β search
SSMax (Nakanishi, 2025) (= M1)	$n \in [1, 1024]$	free	grid
Ours, grid (= M2)	$n \in \{64, \dots, 1024\}$	$\equiv 0$	grid (step 0.05)
Ours, OLS slope	$n \in \{64, 128, \dots, 1024\}$ (six points)	$\equiv 0$	continuous

The body figures Figures 1c and 1d use the grid version of Ours. Figure 5 reports the M2 loss landscape on the same fine grid for all four runs at three training milestones; the rotary runs are added here only as a reference, since the body intentionally does not contrast positional encodings.

Why $a_2 \equiv 0$. The per-(layer, head) realization (A.1) already places a layer-side scalar bias inside the inverse-temperature parameterization. A free a_2 in the post-hoc fit would re-introduce that same bias on top, leaving ξ_β under-identified by the residual curvature of β_n . Empirically, on the trained checkpoints, M1 (a_2 free) selects $\xi_\beta = 1$ in only 3/28 (11%) snapshots and otherwise wanders the grid with no stable trend across iters; the bias absorbs the signal. Forcing $a_2 \equiv 0$ removes this absorption and lets ξ_β identify the residual log-log slope of β_n .

Why $n \geq 64$. The trimming threshold matches the smallest n used by the body’s gap-counting estimator $\hat{\xi}_\Lambda$ of Definitions 4.3 and 4.5, namely $n = 64$ (the smallest of the six n values in Appendix F). Defining $\hat{\xi}_\beta$ on the same domain makes the comparison with $\hat{\xi}_\Lambda$ direct rather than a domain-mismatch artefact; the residual finite- n gap $|\hat{\xi}_\Lambda - \hat{\xi}_\beta|$ is the value reported per cell in Table 2. The first half of the context length $n \leq 50$ also contains the small- n dynamics of β_n that deviate from the asymptotic power family; trimming there isolates the scaling regime that Corollary 4.9 characterizes.

Trim sensitivity. Table 4 reports $\hat{\xi}_\beta$ as the trim threshold varies, on the two absolute-PE runs at iter = 100k. The $n \geq 64$ choice sits in a stable plateau (within ± 0.04 of the $n \geq 51$ value), and pushing the threshold to $n \geq 200$ shifts $\hat{\xi}_\beta$ by ≤ 0.16 on the more sensitive dataset (OpenWebText), consistent with β_n being well approximated by the power family on the asymptotic tail.

B.2 Error-bar widths for the body four-panel figure

The cell-wise relative upper bounds quoted in Figure 1 (SE on PPL $\leq 10\%$ of the cell mean in (a, b); half-IQR on MSE $\leq 8\%$ of the point-estimate MSE in (c, d)) are derived by the protocol below. Each width is the natural sampling uncertainty of the y-axis quantity at that panel type, reduced to a single per-panel number by taking the maximum across the cells (Qwen) or ξ_β grid points (nanoGPT) plotted in the panel.

trim	$n \geq 10$	$n \geq 25$	$n \geq 51$	$n \geq 64$	$n \geq 100$	$n \geq 200$
SlimPajama	0.305	0.336	0.368	0.380	0.410	0.477
OpenWebText	0.375	0.414	0.457	0.474	0.517	0.618

Table 4: $\hat{\xi}_\beta$ from the continuous OLS fit of β_n to $a_1(\log n)^{\xi_\beta}$ on $n \geq \text{trim}$, two absolute-PE training-time GPT-124M runs at iter = 100k. The body uses the discrete six-point variant on $n \in \{64, 128, 256, 512, 768, 1024\}$, which gives $\hat{\xi}_\beta = 0.346$ (SP) and 0.418 (OWT).

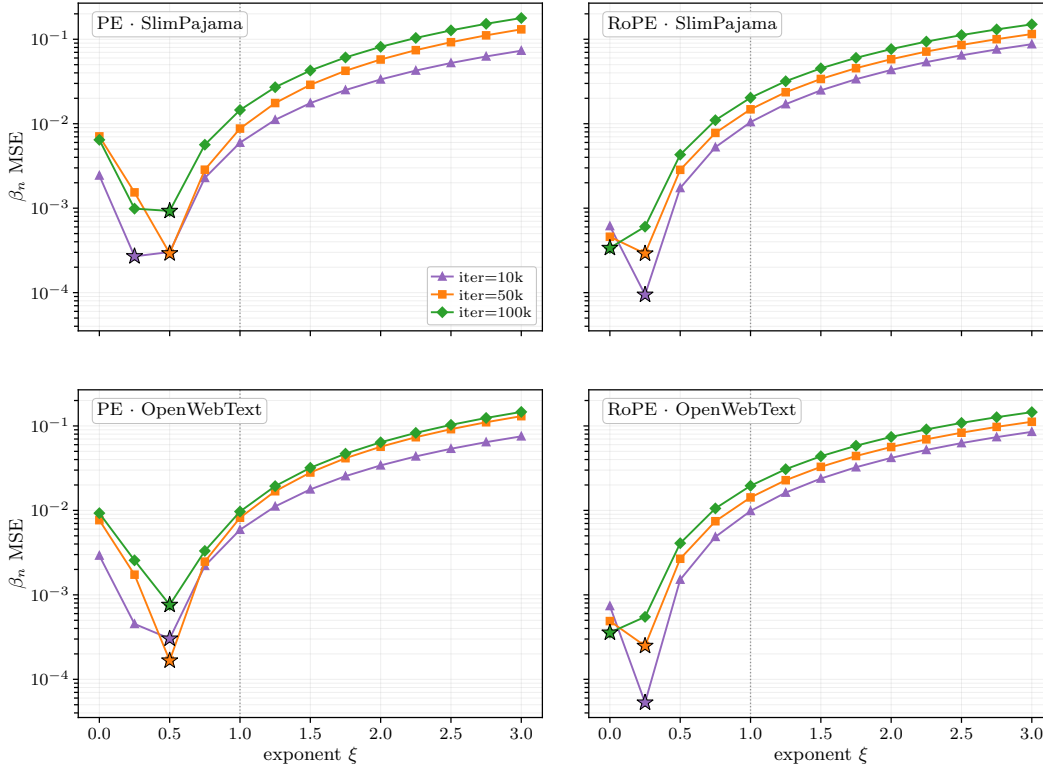


Figure 5: M2 loss landscape on all four training-time GPT-124M runs. The y -axis is the per-point MSE of the bias-free post-hoc least-squares fit of β_n to $a_1(\log n)^{\xi_\beta}$ on $n \geq 64$, on a log scale; one curve per snapshot iter $\in \{10k, 50k, 100k\}$, with stars at per-curve argmin and a dotted vertical reference at the logarithmic value $\xi_\beta = 1$. PE and RoPE runs settle at distinct exponents within each dataset.

Panels (a, b): doc-level standard error on PPL. At each $(\xi_\beta, n_{\text{eval}})$ cell, the body figure plots the per-document strict perplexity $\text{PPL}_{\text{strict}}^{(d)}$ averaged over the n_{doc} documents that fit at that n_{eval} , with $n_{\text{doc}} \in \{14, 15, \dots, 19\}$ on PG-19 and $n_{\text{doc}} = 20$ on Proof-Pile-2 (Appendix A.2). The reported quantity is the doc-level standard error of the cell mean $\text{SE} = s/\sqrt{n_{\text{doc}}}$, where s is the sample standard deviation of $\{\text{PPL}_{\text{strict}}^{(d)}\}_{d=1}^{n_{\text{doc}}}$; the cell-wise maxima of SE/mean across the 35 cells per dataset are 9.52% on PG-19 and 8.79% on Proof-Pile-2 (both attained at $\xi_\beta = 0$, the length-multiplier-off endpoint). The cell-wise medians are 7.49% and 8.04% respectively, so the body’s 10% envelope is loose by less than a factor of 1.3. A per-cell document-resampling bootstrap ($B=200$, percentile half-IQR of the cell mean) gives a tighter 4.95% / 5.32% but is dominated by the more conservative SE-based number quoted in the body caption.

Panels (c, d): residual bootstrap of the M2 MSE curve. At each ξ_β on the body grid, the MSE plotted in (c, d) is a deterministic function of a single trained β_n vector (Appendix B.1); its sampling uncertainty arises from the regression residuals on positions $n \in [64, 1024]$. Let \hat{a}_1 denote the M2 estimate at the given ξ_β and $e_n = \beta_n - \hat{a}_1(\log n)^{\xi_\beta}$ the residual. We resample e_n with replacement across positions $B = 200$ times; for each resample e_n^* we form $y_n^* = \hat{a}_1(\log n)^{\xi_\beta} + e_n^*$, refit a_1 , and recompute the per-point MSE. The width is the half-IQR of these B MSE values divided by the

point-estimate MSE. Across all six (dataset, iter) snapshots (Figure 5), the per-grid maximum of this ratio peaks at 7.29% (SlimPajama, iter = 50k, near $\xi_\beta \approx 0.55$); medians stay between 2.7% and 2.9%.

C Auxiliary results for the deterministic theory

This appendix collects strands deferred from Section 4. Appendix C.1 reduces the supremum (4.3) defining Λ_n to a finite maximum over competitor gaps. Appendix C.2 handles the degenerate case of ties at the maximum. Appendix C.3 gives the score-realizability reduction used throughout Section 4.4: any positive score matrix arises from self-attention with $Q_n = K_n$.

Throughout this appendix we write $\mathcal{U}_n := \{z_n^* - z_{n,j} : 1 \leq j \leq n, z_{n,j} < z_n^*\}$ for the set of positive competitor gaps.

C.1 Discrete representation of Λ_n

Lemma C.1 (Discrete representation of Λ_n). *On the finite- Λ_n domain ($N_n(0) = 1$), the upper-tail accumulation scale of Definition 4.4 satisfies*

$$\Lambda_n = \sup_{t>0} \frac{\log N_n(t)}{t} = \max_{u \in \mathcal{U}_n} \frac{\log N_n(u)}{u}.$$

If $N_n(0) \geq 2$ (ties at the maximum), then $\Lambda_n = \infty$.

Proof. $t \mapsto N_n(t)$ is right-continuous and piecewise constant with jumps only at points of $\{0\} \cup \mathcal{U}_n$, so $\log N_n(t)$ is constant on each interval $[u, u')$ between consecutive points of $\{0\} \cup \mathcal{U}_n \cup \{+\infty\}$, while the denominator t is increasing. Hence $t \mapsto \log N_n(t)/t$ is nonincreasing on each such interval, and the supremum is attained at some $u \in \mathcal{U}_n$. If $N_n(0) \geq 2$, $N_n(t) \geq 2$ for every $t > 0$ and $\log N_n(t)/t \rightarrow \infty$ as $t \downarrow 0$. \square

Sorted-rank rendering. The body figure Figure 2 plots the counting-function view $t \mapsto N_n(t)$. The same data admits an equivalent rendering as the sorted competitor gaps $j \mapsto g_{n,(j)}$, obtained by swapping the two axes $j \leftrightarrow N$: the right-continuous step $N_n(t)$ on $\log y$ maps to the ascending staircase $g_{n,(j)}$ on $\log x$, and the exponential envelope $N = e^{\Lambda_n t}$ inverts to its logarithmic form $t = \log j / \Lambda_n$. The contact point $(\Delta_n, N_n(\Delta_n))$ on the right is the same point (j^*, Δ_n) with $j^* = N_n(\Delta_n)$ on the left, and Lemma C.1's claim that the supremum is attained at a competitor gap is the statement that the sorted-rank staircase touches the envelope on its riser, not its tread. Figure 6 shows both renderings together.

C.2 Ties at the maximum

Corollary C.2 (Ties at the maximum). *Let*

$$n_{\max} := N_n(0) = \#\{j \in \{1, \dots, n\} : z_{n,j} = z_n^*\}.$$

Then:

1. if $n_{\max} \geq 2$, then $\Lambda_n = \infty$;
2. for every $\beta > 0$,

$$\max_j p_{n,j}(\beta) \leq \frac{1}{n_{\max}}, \quad H_n(\beta) \geq \log n_{\max}.$$

In particular, if $n_{\max} \geq 2$ for infinitely many n , then no finite TE scale exists.

Proof. If $n_{\max} \geq 2$, then $z_n^* - z_{n,j} = 0$ for the n_{\max} tokens at the maximum, so $N_n(t) \geq n_{\max}$ for every $t > 0$. Consequently

$$\frac{\log N_n(t)}{t} \geq \frac{\log n_{\max}}{t} \rightarrow \infty \quad (t \downarrow 0),$$

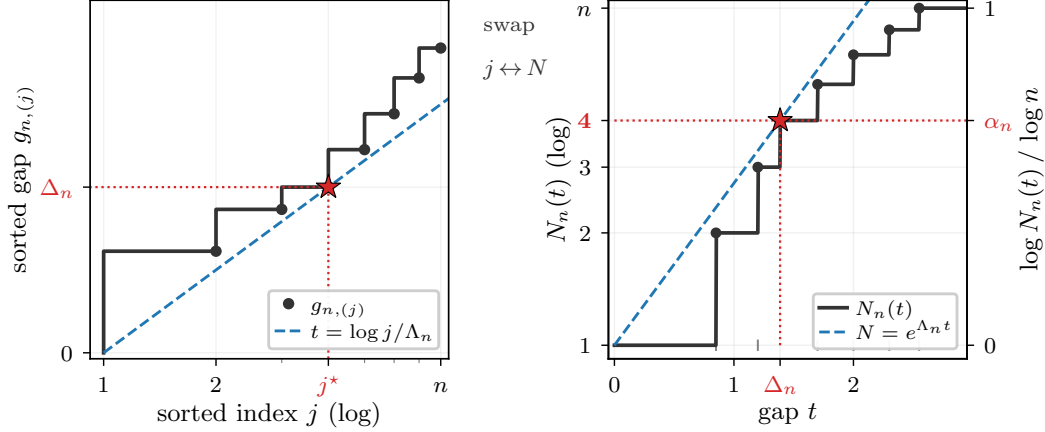


Figure 6: Two equivalent renderings of the same N_n . *Right*: the cumulative gap-count curve $t \mapsto N_n(t)$ on the gap axis $t \geq 0$ and a log y -axis, with the dashed exponential envelope $N = e^{\Lambda_n t}$ (4.2); the red star marks the contact point $(\Delta_n, N_n(\Delta_n))$, and the secondary right axis reads $\alpha_n = \log N_n(\Delta_n) / \log n$. This is the panel reproduced in the body as Figure 2. *Left*: the equivalent sorted-competitor-gap rendering $j \mapsto g_{n,(j)}$ on a log j -axis, with $t = \log j / \Lambda_n$ as the inverse form of the accumulation envelope; the red star sits at the same contact point with horizontal coordinate $j^* = N_n(\Delta_n)$. The two panels are related by the axis swap $j \leftrightarrow N$.

so $\Lambda_n = \infty$ by Definition 4.4. The top n_{\max} softmax coordinates are equal, and their total mass is at most 1, so each of them is at most $1/n_{\max}$. Thus $\max_j p_{n,j}(\beta) \leq 1/n_{\max}$. Since every softmax coordinate is at most $1/n_{\max}$,

$$H_n(\beta) = - \sum_{j=1}^n p_{n,j}(\beta) \log p_{n,j}(\beta) \geq - \sum_{j=1}^n p_{n,j}(\beta) \log(1/n_{\max}) = \log n_{\max}.$$

For the final assertion, suppose $(X_n) \subset (0, \infty)$ is a finite TE scale and set $\beta_n := nX_n$, so $\beta_n/X_n = n \rightarrow \infty$. Then Definition 4.2 forces $H_n(\beta_n) \rightarrow 0$, contradicting $H_n(\beta_n) \geq \log n_{\max} \geq \log 2$ on the infinite subsequence with $n_{\max} \geq 2$. \square

C.3 Score realizability via positive Gram matrices

Definition C.3 (Positive matrix). A matrix $A \in \mathbb{R}^{n \times n}$ is *positive semidefinite* if $x^\top A x \geq 0$ for every $x \in \mathbb{R}^n$. We call A *positive*, and write $A \geq 0$, if A is symmetric and positive semidefinite. Every Gram matrix considered in the sequel is positive in this sense, so we use the predicate $A \geq 0$ throughout.

Proposition C.4 (Gram reduction for positive score matrices). *Let $\Sigma_n \in \mathbb{R}^{n \times n}$ satisfy $\Sigma_n \geq 0$ with $\text{rank } \Sigma_n \leq d_{\text{qk},n}$. Then there exist matrices $Q_n, K_n \in \mathbb{R}^{d_{\text{qk},n} \times n}$ with $Q_n = K_n$ such that the self-attention score matrix equals Σ_n :*

$$\frac{\langle q_{n,i}, k_{n,j} \rangle}{\sqrt{d_{\text{qk},n}}} = (\Sigma_n)_{ij}, \quad 1 \leq i, j \leq n.$$

In particular, every row of Σ_n is realized as a fixed-query self-attention score vector.

Proof. Choose $B_n \in \mathbb{R}^{d_{\text{qk},n} \times n}$ with $B_n^\top B_n = \Sigma_n$, padding by zero rows if necessary. Setting $Q_n = K_n = d_{\text{qk},n}^{1/4} B_n$ gives $Q_n^\top K_n / \sqrt{d_{\text{qk},n}} = B_n^\top B_n = \Sigma_n$. \square

D Rank-collapse boundary and resolved accumulation

The body's TE scale Λ_n controls the top-two/entropy pair via Theorem 4.6 but does not by itself imply coordinate-wise rank collapse (Section 4.1). This appendix records the exact rank-collapse

criterion, defines the corresponding *rank boundary*, identifies the positive-resolution accumulation proxy that sandwiches it, and proves [Corollary 4.7](#).

Define the *rank free energy*

$$\mathcal{F}_n(\beta) := \log Z_n(\beta). \quad (\text{D.1})$$

Proposition D.1 (Exact coordinate-wise rank-collapse criterion). *Let*

$$\mathcal{G}_n(\beta) := \max_{i,j} |p_{n,i}(\beta) - p_{n,j}(\beta)|.$$

For any positive deterministic sequence (β_n) ,

$$\mathcal{G}_n(\beta_n) \rightarrow 0 \iff \mathcal{F}_n(\beta_n) \rightarrow \infty.$$

Equivalently,

$$\max_j \left| p_{n,j}(\beta_n) - \frac{1}{n} \right| \rightarrow 0 \iff \mathcal{F}_n(\beta_n) \rightarrow \infty.$$

Proof. The largest unnormalised softmax weight equals 1, so

$$p_n^*(\beta) := \max_j p_{n,j}(\beta) = \frac{1}{Z_n(\beta)} = e^{-\mathcal{F}_n(\beta)}.$$

Since $\mathcal{G}_n(\beta) \leq p_n^*(\beta)$, the condition $\mathcal{F}_n(\beta_n) \rightarrow \infty$ implies $\mathcal{G}_n(\beta_n) \rightarrow 0$. Conversely, $\min_j p_{n,j}(\beta) \leq 1/n$, hence

$$p_n^*(\beta) \leq \mathcal{G}_n(\beta) + \frac{1}{n}.$$

Thus $\mathcal{G}_n(\beta_n) \rightarrow 0$ implies $p_n^*(\beta_n) \rightarrow 0$, which is equivalent to $\mathcal{F}_n(\beta_n) \rightarrow \infty$.

The coordinate-wise uniform-law equivalence follows from

$$p_n^*(\beta) \rightarrow 0 \iff \max_j \left| p_{n,j}(\beta) - \frac{1}{n} \right| \rightarrow 0,$$

because $1/n \rightarrow 0$ and $0 \leq p_{n,j}(\beta) \leq p_n^*(\beta)$. \square

Definition D.2 (Rank boundary). For $0 \leq r \leq \log n$, define

$$B_n^{\text{rank}}(r) := \sup \{ \beta \geq 0 : \mathcal{F}_n(\beta) \geq r \}.$$

[Proposition D.1](#) implies that coordinate-wise rank collapse holds along (β_n) if and only if there exists $r_n \rightarrow \infty, r_n \leq \log n$, such that

$$\beta_n \leq B_n^{\text{rank}}(r_n)$$

eventually.

Definition D.3 (Resolved accumulation scale). For $r \geq 0$, define

$$\Lambda_n^{(r)} := \sup_{t > 0: \log N_n(t) > r} \frac{\log N_n(t) - r}{t},$$

with the convention $\sup \emptyset = 0$.

At zero resolution,

$$\Lambda_n^{(0)} = \Lambda_n.$$

Thus the upper-tail accumulation scale of the body is the *zero-resolution accumulation scale*. The rank-collapse boundary is obtained by taking a positive diverging resolution $r_n \rightarrow \infty$, which removes finite near-tie clusters from the envelope.

Proposition D.4 (Resolved accumulation implies rank-gap collapse). *Let $r_n \rightarrow \infty$. If*

$$\beta_n < \Lambda_n^{(r_n)}$$

eventually, then $\mathcal{G}_n(\beta_n) \rightarrow 0$.

Proof. By the definition of $\Lambda_n^{(r_n)}$, for all large n there exists $t_n > 0$ such that

$$\beta_n t_n < \log N_n(t_n) - r_n.$$

The $N_n(t_n)$ tokens within gap t_n each contribute at least $e^{-\beta_n t_n}$ to the partition function. Hence

$$Z_n(\beta_n) \geq N_n(t_n) e^{-\beta_n t_n} > e^{r_n}.$$

Since $r_n \rightarrow \infty$, [Proposition D.1](#) gives $\mathcal{G}_n(\beta_n) \rightarrow 0$. \square

Define the Laplace envelope

$$S_n(\beta) := \sup_{t \geq 0} \{\log N_n(t) - \beta t\}. \quad (\text{D.2})$$

Lemma D.5 (Laplace-envelope sandwich). *For every $\beta > 0$,*

$$S_n(\beta) \leq \mathcal{F}_n(\beta) \leq S_n(\beta) + \log(1 + \log n).$$

Proof. For the lower bound, fix $t \geq 0$. The $N_n(t)$ tokens with gap at most t each contribute at least $e^{-\beta t}$, hence

$$Z_n(\beta) \geq N_n(t) e^{-\beta t}.$$

Taking the supremum over t gives $S_n(\beta) \leq \mathcal{F}_n(\beta)$.

For the upper bound, write the ordered competitor gaps as $0 = t_{n,1} \leq t_{n,2} \leq \dots \leq t_{n,n}$. Since $N_n(t_{n,j}) \geq j$, the definition of S_n implies

$$\log j - \beta t_{n,j} \leq S_n(\beta).$$

Thus

$$e^{-\beta t_{n,j}} \leq \frac{e^{S_n(\beta)}}{j}.$$

Summing over j gives

$$Z_n(\beta) \leq e^{S_n(\beta)} \sum_{j=1}^n \frac{1}{j} \leq e^{S_n(\beta)} (1 + \log n).$$

Taking logarithms proves the upper bound. \square

Consequently, for $r > \log(1 + \log n)$,

$$\Lambda_n^{(r)} \leq B_n^{\text{rank}}(r) \leq \Lambda_n^{(r - \log(1 + \log n))}.$$

Therefore, at resolutions $r_n \gg \log \log n$, the exact rank boundary is described by the resolved accumulation scale up to the envelope discretisation error $\log(1 + \log n)$.

Corollary D.6 (Contact-count entropy criterion for rank collapse). *Assume $\beta_n/\Lambda_n \rightarrow 0$. If the contact-count entropy $C_n := \log N_n(\Delta_n) = \Lambda_n \Delta_n$ satisfies $C_n \rightarrow \infty$, then $\mathcal{G}_n(\beta_n) \rightarrow 0$.*

Proof. Set $s_n = \beta_n/\Lambda_n$. The contact gap Δ_n gives

$$Z_n(\beta_n) \geq N_n(\Delta_n) e^{-\beta_n \Delta_n} = \exp\{(1 - s_n) C_n\}.$$

Since $s_n \rightarrow 0$ and $C_n \rightarrow \infty$, the right-hand side diverges. [Proposition D.1](#) applies. \square

Proof of Corollary 4.7. The supercritical implication is the supercritical direction of [Theorem 4.6](#) and uses no contact-count hypothesis. The subcritical implication is exactly [Corollary D.6](#). \square

Example D.7 (Finite contact count: TE and RE scales separate). The condition $C_n \rightarrow \infty$ in [Corollary 4.7](#) cannot be dropped: the score family below has $C_n = \log 2$ (bounded) and rank collapse fails, even though (Λ_n) is the TE scale. Set

$$z_{n,1} = 0, \quad z_{n,2} = -\frac{\log 2}{\log n}, \quad z_{n,j} = -\log n \quad (j \geq 3),$$

so that $z_n^* = 0$ and the competitor gaps are $z_n^* - z_{n,2} = (\log 2)/\log n$ and $z_n^* - z_{n,j} = \log n$ for $j \geq 3$. Then $\Lambda_n = \log n$, $\Delta_n = (\log 2)/\log n$, and $\alpha_n = (\log 2)/\log n \rightarrow 0$. With $\beta_n = \sqrt{\log n}$ so that $\beta_n/\Lambda_n \rightarrow 0$, the softmax row converges to $(\frac{1}{2}, \frac{1}{2}, 0, \dots, 0)$: top-two collapse holds, but the limit is not the uniform law and rank collapse fails. A rank-resolved analysis is given in [Example D.8](#).

dataset	n_{eval}	median p_n^* at $\beta = \gamma\Lambda_n$			frac. $p_n^* \leq 1/\log n$
		$\gamma = 0.5$	$\gamma = 1.0$	$\gamma = 1.5$	at $\gamma = 0.1$
PG-19	16384	0.20	0.45	0.64	89%
PG-19	32768	0.17	0.42	0.63	91%
Proof-Pile-2	16384	0.18	0.42	0.63	89%
Proof-Pile-2	32768	0.15	0.40	0.62	93%

Table 5: Boundary check via $p_n^*(\gamma\Lambda_n)$ on Qwen-7B-Chat attention rows at $\xi_0 = 2$ (45,467 rows total across the four cells, exact-tie rows excluded). Median p_n^* at $\gamma \in \{0.5, 1.0, 1.5\}$ and per-cell fraction with $p_n^* \leq 1/\log n$ at $\gamma = 0.1$. On the wider sweep $\gamma \in \{0.1, 0.25, 0.5, 0.75, 1.0, 1.5, 2.0, 4.0\}$ the median p_n^* is monotone in γ on every cell, ranging from ~ 0.001 at $\gamma = 0.1$ to ~ 0.96 at $\gamma = 4$, and the same monotonicity holds on the nanoGPT cells.

Example D.8 (Rank-resolved analysis of the finite-contact case). For the score family of [Example D.7](#), $\Lambda_n = \log n$ because the contact gap $\Delta_n = (\log 2)/\log n$ attains the zero-resolution envelope. The two competitor gap levels satisfy $\log N_n((\log 2)/\log n) = \log 2$ and $\log N_n(\log n) = \log n$. For any $r_n \rightarrow \infty$ with $r_n = o(\log n)$, eventually $r_n > \log 2$, so the contact gap Δ_n is excluded by the constraint $\log N_n(t) > r_n$ in [Definition D.3](#), leaving only $t = \log n$:

$$\Lambda_n^{(r_n)} = \frac{\log n - r_n}{\log n} \sim 1.$$

Thus the TE scale is order $\log n$, while the rank-resolved accumulation scale is order one. With $\beta_n = \sqrt{\log n}$, $Z_n(\beta_n) \rightarrow 2$ and $\mathcal{G}_n(\beta_n) \rightarrow \frac{1}{2}$.

D.1 Empirical instances on the verification cells

The verification cells of [Table 2](#) occupy two distinct regimes of [Corollary 4.7](#).

TE-to-RE upgrade. [Theorem 4.6](#) identifies Λ_n as the TE scale unconditionally; the upgrade to RE scale via [Corollary 4.7](#) requires the contact-count entropy $C_n = \alpha_n \log n$ to diverge, equivalently $\xi_\alpha > -1$. The four nanoGPT cells of [Table 2](#) have $\hat{\xi}_\alpha \in (-1.04, -0.86)$, so the relaxed condition holds with $1 + \hat{\xi}_\alpha > 0$ giving a slow $C_n \asymp (\log n)^{1+\hat{\xi}_\alpha}$ divergence. The four Qwen cells have $\hat{\xi}_\alpha \in (-1.69, -1.40)$ on the observed window; since $C_n \geq \log 2$ always, the bucket-mean slope $\hat{\xi}_\alpha < -1$ cannot persist asymptotically, and the analytical RE-scale upgrade of [Corollary 4.7](#) does not directly apply, with the rank-resolved boundary of [Proposition D.1](#) as the formal substitute. The empirical boundary character of Λ_n on these cells is then verified directly below.

Boundary check on Λ_n . Independently of the analytical sufficient condition, the boundary character of Λ_n can be tested by reading the per-row maximum softmax weight $p_n^*(\beta) = 1/Z_n(\beta)$ at $\beta = \gamma\Lambda_n$ on a sweep around criticality. [Table 5](#) reports the median p_n^* at $\gamma \in \{0.5, 1.0, 1.5\}$ and the per-cell fraction of rows with $p_n^* \leq 1/\log n$ at $\gamma = 0.1$ (strict subcritical) on the four Qwen cells. Across all cells the median traces a smooth monotone curve from $\sim 10^{-3}$ at $\gamma = 0.1$ to ~ 1 at $\gamma = 4$, crossing ~ 0.42 at $\gamma = 1$, with $\sim 90\%$ of rows below $1/\log n$ at $\gamma = 0.1$ and 0% at $\gamma \geq 1$. The framework’s Λ_n separates the subcritical-collapse regime from the supercritical-concentration regime empirically, including on the Qwen cells where the contact-count entropy is bounded and [Corollary 4.7](#) does not directly apply. [Example D.7](#) shows that this analytical upgrade is sharp in the worst case (a contrived score family with C_n bounded fails rank collapse), but the Qwen rows in the bounded- C_n regime do not realize that pathology at the operating β .

E Derivation of the YaRN inverse-temperature scaling

This appendix spells out why the YaRN context-window extension of [Peng et al. \(2023\)](#) produces an effective inverse-temperature scaling $\beta_n \asymp (\log n)^2$, i.e. implicit exponent $\xi = 2$ in the parameterisation of [Section 2.2](#).

[Peng et al. \(2023\)](#) replace the standard softmax logit $q_m^\top k_n / \sqrt{d}$ with $q_m^\top k_n / (t\sqrt{d})$ for a length-dependent temperature $t = t(s)$, where $s = n/n_{\text{train}}$ is the ratio of the target context length n to the

training window n_{train} . The recommended schedule (their §3.3) is

$$\frac{1}{\sqrt{t(s)}} = 1 + 0.1 \ln s,$$

and the multiplier $1/\sqrt{t(s)}$ is *multiplied onto the rotary embeddings of both the query and the key*. Substituting into the logit gives a rescaling

$$\beta_n \propto 1/t(n/n_{\text{train}}) = (1 + 0.1 \ln(n/n_{\text{train}}))^2 \asymp (\log n)^2,$$

i.e. a scalar multiplier $\asymp (\log n)^2$ asymptotically. The fact that the multiplier is applied to both sides of the inner product, rather than once, is what doubles the exponent relative to a log n -only temperature, and places YaRN in the $\xi = 2$ row of [Table 1](#).

F Training-time exponent measurement: acquisition protocol, per-seed granularity, and limitations

This appendix gives the per-row gap-counting acquisition protocol, the β_n regression-fit protocol, and limitations for the training-time consistency check of [Section 4.5.1](#). The upstream training setup that produces the learnable inverse-temperature vector β_n being measured here, namely the models, datasets, four-configuration schedule, and the per-(layer, head) realization ([A.1](#)), is documented in [Appendix A.3](#); the body β_n regression fit itself is in [Appendix B.1](#).

Gap-counting estimator $\hat{\xi}_\Lambda$. We analyse the four training-time GPT-124M runs (two PE datasets, two RoPE) of [Appendix A.3](#) at the seven milestone checkpoints. For each checkpoint, three evaluation seeds produce independent validation batches ($B = 16$ sequences, context lengths $n \in \{64, 128, 256, 512, 768, 1024\}$, block size 1024). For each (layer, head, n , batch) row we record the current-layer dot product $z_{n,j} = \langle q, k_j \rangle / \sqrt{d}$ with $z_n^* := \max_j z_{n,j}$. Per-row Λ_n and the contact coordinates (α_n, Δ_n) are computed from [Definition 4.5](#) via the competitor gaps $z_n^* - z_{n,j}$ at numerical tolerance $\epsilon = 10^{-6}$. The body’s $\hat{\xi}_\Lambda$ is the bucket-mean slope estimator of [Section 4.5.1](#): rows are pooled across evaluation seeds into the index sets $\mathcal{R}(c, n)$, the bucket mean is taken over those pooled rows at each of the six n values, and $\hat{\xi}_\Lambda$ is the OLS slope of those bucket means against $\log \log n$. Because each of the three seeds contributes the same $(\ell, h, \text{batch}, n)$ structure, the pooled-row slope coincides with the mean of three per-seed slopes; the body’s headline half-width is the bootstrap-IQR/2 over (s, ℓ, h) tuples of [Section 4.5.1](#). Rows with $\log_{10} \Lambda_n > 5$ (exact-tie configurations) are dropped before averaging, matching the Qwen protocol of [Appendix G.1](#).

Bootstrap intervals. For each cell c let $\mathcal{T}(c)$ be the cell’s bootstrap-unit set: $\{(\ell, h)\}$ on Qwen and $\{(s, \ell, h)\}$ on nanoGPT, the latter pooled across the three evaluation seeds. Each draw selects $|\mathcal{T}(c)|$ tuples uniformly with replacement from $\mathcal{T}(c)$, recomputes the bucket-mean slope $\hat{\xi}_X(c)$ from the rows in $\mathcal{R}(c, n)$ that belong to the drawn tuples (separately at each $n \in \mathcal{N}(c)$), and the half-IQR over $B = 200$ such draws is the half-width reported in [Table 2](#); tie % follows the same convention. The ξ_β^* column carries no interval on Qwen (0.5-grid PPL minimum) and the six-point OLS standard error of $\hat{\xi}_\beta$ on nanoGPT.

β_n -fit estimator $\hat{\xi}_\beta$. At every checkpoint β_n is read off the model state and fitted to the bias-free power family $\beta_n = a_1 (\log n)^{\xi_\beta}$ at the same six n that the gap-counting uses. The OLS slope of $\log \beta_n$ on $\log \log n$ at those six points yields $\hat{\xi}_\beta$ (closed-form least squares, no grid). The shared domain matters: [Theorem 4.6](#) predicts equality of $\hat{\xi}_\Lambda$ and $\hat{\xi}_\beta$ in the limit, but only when both estimators are read on the same n set; this is the choice we make throughout. The bias-free constraint $a_2 \equiv 0$ is justified in [Appendix B.1](#).

Limitations. The check is limited in two respects. (i) *Single training seed per configuration.* The $\hat{\xi}_\Lambda$ band is over three evaluation batches at fixed training seed; variation from initialisation and data ordering is not measured. $\hat{\xi}_\beta$ has no eval-seed variance by construction. (ii) *Short context.* With $n \leq 1024$ the log-log dynamic range covers half a decade, which constrains the bucket-mean slope but leaves higher-order curvature unconstrained; this is part of why $\hat{\xi}_\Lambda$ and $\hat{\xi}_\beta$ retain a finite- n gap.

G Acquisition protocol for the verification analysis on Qwen-7B-Chat

This appendix records the per-row attention acquisition pipeline that backs the verification analysis of Section 4.5 and the body figures it feeds.

G.1 Acquisition protocol

We use Qwen-7B-Chat with dynamic-NTK RoPE enabled (Appendix A.2). Attention rows are collected from all 32 layers and 32 heads on PG19 and Proof-Pile-2 at context lengths $n_{\text{eval}} \in \{8192, 16384, 32768\}$, with four context-length values per document at the ratios $n/n_{\text{eval}} \in \{1/4, 1/2, 3/4, 1\}$ and one query position per (layer, head, document, n) tuple. The body’s per- n_{eval} fit of Section 4.5.1 skips $n_{\text{eval}} = n_{\text{train}} = 8192$ (training window, no extrapolation). The upstream pass applies a length-dependent inverse-temperature multiplier $\beta_n \propto (\log n)^{\xi_0}$ at the seven values $\xi_0 \in \{0, 0.5, 1, 1.5, 2, 2.5, 3\}$, where $\xi_0 = 0$ disables the multiplier; ξ_0 perturbs the representation entering a layer while the measured object is always the unrescaled current-layer score $z_{n,j} = \langle \mathbf{q}_{n,i_n}, \mathbf{k}_{n,j} \rangle / \sqrt{d_{qk}}$. Across the three context lengths and four ratios, this yields eight values $n \in \{2048, 4096, 6144, 8192, 12288, 16384, 24576, 32768\}$. The published-paper headline aggregation (Section 4.5.1 and Table 2) uses the document subset 4 from PG-19 and 5 from Proof-Pile-2, so the total attention-row count entering the headline statistics is $32 \times 32 \times 3 (n_{\text{eval}}) \times 4$ (ratios) $\times 7 (\xi_0) \times (4+5)$ (docs) = 774,144. The empirical contact gap is the largest competitor gap u satisfying $\log N_n(u)/u \geq (1 - \epsilon) \Lambda_n$ at $\epsilon = 10^{-6}$, a floating-point relaxation of the exact maximizer in Definition 4.5.

Per- n_{eval} fit. The body $\hat{\xi}_{\text{pool}}(n_{\text{eval}})$ is the OLS slope of the count-weighted means of $\log \Lambda_n$ taken at each of the four n values within an n_{eval} , regressed against $\log \log n$. Sink-token attention rows with $\log_{10} \Lambda_n > 5$ are excluded from the bulk before averaging. Aggregating across n_{eval} at shared n mixes three dynamic-NTK RoPE rescale conditions (one per source n_{eval}) and biases the slope; per- n_{eval} fits avoid this contamination.

Representative rows shown in body figures. The single attention rows recast as $N_n(t)$ in Figure 4 (middle, right) are selected deterministically from the protocol above: for each contrast cell c , take the row whose $(\log \alpha_n, \log \Delta_n)$ is closest to the cell’s bucket mean $(\overline{\log \alpha}(c, n), \overline{\log \Delta}(c, n))$ in $(\log \alpha_n, \log \Delta_n)$ at the largest $n \in \mathcal{N}(c)$. The two cells used in body Figure 4 are Qwen-7B-Chat PG-19 at $n_{\text{eval}} = 32768$ ($n = 32768$) and nanoGPT SlimPajama at iter = 100k ($n = 1024$); the contact statistics of the selected rows are $(\hat{\Lambda}_n, \hat{\alpha}_n, \hat{\Delta}_n) \approx (4.22, 0.13, 0.33)$ and $(1.64, 0.26, 1.09)$ respectively.